# OPTICAL AND MECHANICAL QUANTUM CONTROL OF NITROGEN VACANCY CENTERS IN DIAMOND

by

MAYRA MAGALI AMEZCUA

A DISSERTATION

Presented to the Department of Physics
and the Graduate School of the University of Oregon
in partial fulfillment of the requirements
for the degree of
Doctor of Philosophy

June 2018

DISSERTATION APPROVAL PAGE

Student: Mayra Magali Amezcua

Title: Optical and Mechanical Quantum Control of Nitrogen Vacancy Centers in Diamond

This dissertation has been accepted and approved in partial fulfillment of the requirements for the Doctor of Philosophy degree in the Department of Physics by:

| | |
|---|---|
| Benjamin McMorran | Chair |
| Hailin Wang | Advisor |
| Steven van Enk | Core Member |
| Spencer Chang | Core Member |
| Jim Prell | Institutional Representative |

and

| | |
|---|---|
| Sara D. Hodges | Interim Vice Provost and Dean of the Graduate School |

Original approval signatures are on file with the University of Oregon Graduate School.

Degree awarded June 2018

DISSERTATION ABSTRACT

Mayra Magali Amezcua

Doctor of Philosophy

Department of Physics

June 2018

Title: Optical and Mechanical Quantum Control of Nitrogen Vacancy Centers in Diamond

Current proposals for the design of quantum computer architectures include combining different quantum systems with designated tasks to build a device that can efficiently store, process, and transfer quantum information. Electron spins in solid-state quantum systems are a viable platform for storing information in these multi-quantum frameworks. While extensive research has been performed to couple solid-state systems to photons and microwaves, an alternative line of research focuses on coupling these systems to phonons, or mechanical motion. The use of phonons in solid-state devices opens up a new approach to interface different quantum systems.

This dissertation presents experimental progress in developing and controlling a spin-mechanical system, specifically the interaction between the electron spin of a nitrogen vacancy (NV) center in diamond and mechanical vibrations on the surface of the diamond, and discusses theoretical methods for limiting decoherence in the system. To investigate the strain properties of the NV center, we couple acoustic waves to the NV spin via an optical excitation. We transfer population between the spin ground states by driving phonon-assisted optical transitions and demonstrate the formation of a non-radiative state, which can be used to adiabatically transfer population between two states, through the same mechanism. To mitigate the effects

of the nuclear spin bath on the NV center, we study and show preliminary results on the semiclassical dressed states, or quantum states of the NV interacting with optical fields. The dressed states can be insensitive to magnetic fluctuations, thus preserving the quantum state of the system. Finally, we consider a transitionless quantum driving technique that decouples the NV center from a radiative state, preventing decoherence through spontaneous emission. These developments are essential in advancing our understanding of phonon-based interfaces between quantum systems.

This dissertation includes previously published and unpublished co-authored material.

CURRICULUM VITAE

NAME OF AUTHOR: Mayra Magali Amezcua

GRADUATE AND UNDERGRADUATE SCHOOLS ATTENDED:
University of Oregon, Eugene, Oregon
Pomona College, Claremont, California

DEGREES AWARDED:
Doctor of Philosophy, Physics, 2018, University of Oregon
Bachelor of Arts, Physics, 2012, Pomona College

AREAS OF SPECIAL INTEREST:
Quantum Optics
Quantum Information
Defect Centers in Diamond

PROFESSIONAL EXPERIENCE:

Graduate Research Fellow, University of Oregon, 2016-2018

Graduate Teaching Fellow, University of Oregon, 2012-2016

Teaching Assistant, Pomona College, 2011

Summer Undergraduate Research Fellow, Pomona College, 2009-2010

GRANTS, AWARDS AND HONORS:

Oral Presentation Award at National SACNAS Conference (2015)

Fall Physics Qualifying Exam Award at University of Oregon (2014)

Weiser Senior Teaching Assistant Award at University of Oregon (2014)

PUBLICATIONS:

Mayra Amezcua, Andrew Golter, and Hailin Wang, Shortcut to Adiabaticity for an Electron Spin in Diamond, presented at Quantum Electronics and Laser Science Conference (CLEO: QELS), San Jose, CA, May 14-19, 2017

Mayra Amezcua, Abigail Pauls , Spencer Alexander , Hailin Wang, Shortcut to Adiabatic Passage in a NV Center, presented at APS March Meeting, New Orleans, LA, Mar. 13-17, 2017

Golter, D. A.,Oo, T., Amezcua, M., Stewart, K. A. Wang, H. Coupling a Surface Acoustic Wave to an Electron Spin in Diamond via a Dark State. Phys. Rev. X 6, 41060 (2016).

Golter, D. A., Oo, T., Amezcua, M., Stewart, K. A. Wang, H. Optomechanical Quantum Control of a Nitrogen-Vacancy Center in Diamond. Phys. Rev. Lett. 116, 143602 (2016)

# ACKNOWLEDGEMENTS

Graduate school has been an interesting experience to say the least. I have learned everything I ever wanted to know about two level systems, that diamonds with defects are good for research, how to communicate science (which I will attempt here), and that 95% of my job was making sure cables were plugged in correctly, enough filters were in the beam path and that the timing of my experiment was precise. I have made it this far thanks to the support of my family, friends, advisor, professors, and labmates.

First and foremost, I would like to thank my family for their love, prayers, and encouragement during my PhD program. Special thanks to my Mom and Dad for always putting my needs first and providing me with all the resources to succeed. My wonderful brother, Tony, always found a way to make me smile and keep me sane during these trying times. I don't know what I would do without him. The Amezcua family and the Castelazo family have been my loudest cheerleaders and they always have thoughtful loving words to share.

I have been blessed with meeting Stephanie Majewski at the University of Oregon. Without her words of encouragement and fiery enthusiasm, I would have quit graduate school a long time ago. She has been instrumental in shaping my graduate experience and helping me get ahead in life.

I would like to thank my advisor, Hailin Wang for the unique experience. He has been patient and kind throughout this whole process, especially when I changed the jet angle of the dye laser and we spent all spring break getting it to lase. I would like to express my gratitude to my colleagues from the Wang lab. Andrew Golter is an inspiration of what a good grad student looks like and we have had many fruitful

discussions. Tom Baldwin has been a wonderful mentor and friend. He has taught me so much and I am eternally grateful for all of the python code he left behind. Thein Oo has been a great friend and helped me out numerous times by providing tea, optics wisdom, or exercises to relieve back pain. I have nothing but respect and admiration for Mark Kuzyk, who always finds time to help me with theory and code. Lab would be quite boring without Ignas Lekavicius' political remarks and long rants. He is the best lab mate ever, everyone knows it. Thank you for the rest to the rest of the Wang Lab.

I also want to thank my committee members Ben McMorran, Steven van Enk, Spencer Chang, and Jim Prell for their support throughout my doctoral program. I really hope they read my thesis and find all of the Easter eggs.

I have many friends in the University of Oregon physics department whose advice and support have been invaluable. Ryan Baker has been by my side offering words of encouragement and sharing this long and arduous journey with me. A special thanks to Rudy Resch for assisting me with technical problems, letting me borrow equipment, and providing numerous memes to cheer me up. Thank you to my cohort for making grad school more manageable, especially Wes Erickson, Ian Snyder, Saba Moslehi, Blake Parris, and Gabriel Barello. Thank you to Brandy Todd, Erin Mondloch, Kyle Klarup, Dash Vitullo, Jonathan Mackrory, Roger Smith, Chris Jackson, Dileep Reddy, and many others.

Thank you to my Pomona friends for keeping in touch and sending tea, chocolate, and Korean face products to help me cope with graduate school. Thuy Wong and Rachel Lee are the best friends a girl could ask for.

Finally, a special thanks to my primary undergrad thesis advisor Alfred Kwok for constantly believing in me.

In loving memory of Alfred Kwok.

TABLE OF CONTENTS

LIST OF FIGURES

Figure Page

# CHAPTER I

# INTRODUCTION

For over 50 years, scientists have been intrigued with impurities embedded in the diamond lattice. The diamond is a notable host because of its remarkable properties, such as hardness, thermal conductivity, and chemical inertness. The diamond's large band gap (5.5eV) creates a wide transparency window which supports defects with optical transitions [97]. In fact, the diamond features over 100 fluorescent defects from which a significant fraction have been analyzed [53] but only a few are studied in depth for their potential applications. Nitrogen is the most abundant impurity in diamond, existing in substitutional and aggregated form [66]. One of the most prominent examples is the nitrogen vacancy center because it is a valuable spin platform for research into quantum technologies and metrology.

The nitrogen vacancy is well known for its unique and exceptional properties both at room and cryogenic temperatures. The most fascinating feature of the NV center is the ability to initialize and readout the electron spin optically, even at room temperature. The bright fluorescence of the defect allows for imaging and control to be carried out with a home-built confocal microscope. The ground state energy levels can be coherently manipulated with microwave fields and electron-spin resonance (ESR) techniques. At low temperatures, the excitation spectrum reveals a narrow zero-phonon line (ZPL) with a fine structure which can be employed for all optical control of the spin states. NV centers have one of the longest coherence times $T_2 \approx 2$ ms of solid-state spin systems in ambient conditions [10–12, 116]. Solid-state processing from the semiconductor industry are suitable for diamond. Techniques such as chemical vapor deposition, ion irradiation and annealing, ion beam milling,

and reactive ion etching optimize the production of stable NV centers and promote on-chip optical waveguides [7, 100, 115, 119, 120, 154]. Finally, the electronic orbital states are susceptible to magnetic fields, electric fields, and strain, making it a strong candidate for sensing and exploration of different degrees of freedom.

Optically detected magnetic resonance (ODMR) has become the backbone of many NV related studies due to the possibilities of optical state preparation and spin selective readout. One of the most popular uses of ODMR spectroscopy is for detecting DC, AC, and fluctuating magnetic fields [58, 139]. The direct correlation between magnetic fields and the ground states, and to a lesser extent the excited states, has opened the door to the field of magnetometry using NV centers. Several sensing architectures have been proposed and studied: single NV centers in a nanodiamond on a cantilever [27], arrays of NV centers in bulk crystal or nanocrystals [137, 139], and NV ensembles in a bulk substrate [2]. Other studies have investigated the response of the electron spin to electric fields [38, 39], crystal strain [90, 98, 112, 140], and temperature [1, 106, 144] using ODMR. NV centers in diamond have become so versatile that they have applications in optical magnetic imaging and thermometry in living cells [9, 77, 80].

The main motivation for studying nitrogen vacancy centers is that they are a unique system for exploring the physics and application of quantum control in relatively simple quantum systems. These 'atom-like' systems lend themselves to optical and microwave quantum control, including Rabi oscillation experiments, adiabatic passage, and quantum logic operations. The photon emission process in the NV center is very stable, proving to be a good source of single photons for potential applications in quantum key distribution [48] and quantum computation with linear optics [71]. Quantum interference [133] and entanglement [17] has been demonstrated

between two remote NVs using single photons from the ZPL. One of the major areas of research involving NV centers is their role as a quantum bit, or qubit, for quantum information processing (QIP) devices and other prospective applications [34, 82]. In addition, electron spins associated with the defects in diamond can couple strongly to nearby nuclei spins, potentially enabling the use of nuclear spins for quantum memory at room temperature. Specifically, the electron spin associated with the NV can be coupled to nearby $^{13}$C nuclear spins via hyperfine interactions. This type of couplings has been used for the demonstration of entanglement between nuclear spins [107]. The electron spin has also been coupled to $^{14}$N through microwave transitions for storing and retrieving quantum states [42]. Recently, there has also been growing interest in probing phonon processes in the quantum regime by coupling the NV electron spin to the mechanical motion of a nano-mechanical resonator.

This thesis focuses on experimental studies that extend quantum control of single NV centers beyond the traditional optical and microwave techniques. These experiments employ surface acoustic waves and exploits the coupling between mechanical strain and NV excited states for the quantum control of NV centers.

### 1.1. Solid-State Qubits

The quantum bit, or qubit, can be in a superposition of two states at the same time. This fundamental property of quantum mechanics is key to understanding and controlling quantum processes. The qubit, in its simplest form, can be physically realized as a two-state quantum system. Because of this simple definition, a variety of two-level quantum systems have already been demonstrated in various systems, such as trapped ions [56, 70, 83], quantum dots [60, 89], superconducting circuits [19, 153], color centers in diamond [28, 159], photons [108, 148], silicon carbide [72], and

donor electron spin in silicon [67, 117]. While many of these qubit schemes are being pursued, however, trapped ions and superconducting circuits are the two leading qubit platforms that have been successfully implemented in elementary quantum computers [87].

Similar research efforts continue with spins in solid-state systems. Physical models developed for trapped ions can potentially be adapted to solid-state devices. Current fabrication methods facilitate control of solid-state parameters and promote monolithic circuit design for on-chip devices. Thanks to advances in implantation techniques, solid-state qubits can be deterministically embedded in bulk [86, 110]. Unlike superconducting circuits, defects in solid-state systems exhibit long coherence times [28] for high fidelity gates and information storage.

In this dissertation we study one of the leading solid-state qubit candidates, the negatively charged nitrogen vacancy center in diamond. As discussed earlier, the electron spin associated with the NV center features significantly longer coherence times than competing technologies, and can be even longer when coupled to a nearby nuclear spin [41, 42, 96]. The special properties of the NV center allow photonic networks to be built on-diamond for conveniently initializing, manipulating, and reading-out the system. Crystal strain affects the orbital structure of the NV center, generating a coupling mechanism between phonons and the spin. Spin-phonon systems can be used for long-range interactions between NVs and to cool a mechanical resonator to its ground state [82].

There are two major drawbacks of using NV centers for QIP devices. These are the scalability issue and decoherence. If NV centers in diamond are to become a component of quantum computing architecture in the future, they will need to be

combined with other quantum systems which accomodate their weakness, creating systems known as 'Hybrid Quantum Systems.'

## 1.2. Hybrid Quantum Systems

Sparked by successes in nanomechanical systems [21, 109], a different line of research investigates spin-mechanical systems, in which mechanical resonators mediate the interaction between qubits [29, 122] and qubits are used to create and detect quantum mechanical states [25, 81, 113, 147]. Drawing from proposals on a microwave quantum bus [76, 93, 114, 130, 142], the mechanical quantum bus mediates interactions based on surface acoustic waves (SAW) [131].

SAWs are mechanical waves that propagate along the surface of the material and penetrate one wavelength into the solid. While photons have been reliably used to transmit information, phonons offer special advantages. For example, mechanical waves are better suited for on-chip communication because of their slower velocities and physical confinement in the solid. Their longer wavelength makes it easier to fabricate phononic devices.

SAWs have previously been used and well developed in the classical regime, making them useful for controlling qubits. SAW based devices are commonly used in modern electronic circuits to provide different functions such as filters, transformers, and delay lines [104]. SAW sensors have been used to measure the properties of solids and have expanded to the field of microfluidics [132]. Previous research demonstrated coupling between SAWs and artificial atoms, such as quantum dots [157] and superconducting qubits [55].

The motivation for the development of spin-mechanical systems in NV centers has deep roots in ground state cooling [69, 121] and coherent interactions between

qubits [16, 122], with HQSs gaining interest in recent years [78, 131]. Initial efforts in coupling the electron spin of the NV with a nanomechanical oscillator were through magnetic gradients [4, 74, 121, 122]. Direct coupling between mechanical vibrations in the diamond and the ground state spin were furthered by two types of oscillators: single crystal cantilevers and electrically driven acoustic resonators. In the former method, the cantilever induces energy level shifts when it is bent, allowing strain coupling to the electron spin [13, 112, 140]. The second technique uses a High-Overtone Bulk Acoustic Resonator (HBAR) to generate stress waves which can drive magnetically forbidden transitions [90, 92].

Our research, however, will be to investigate electron-phonon interactions via optical transitions by coupling the spin of a single NV center to a surface acoustic wave. [50, 51]. By using the excited states, we can demonstrate strong coupling with weak fields because optical transitions exhibit direct coupling to the deformation potential [3]. This optomechanical control can be used to cool a diamond nanomechanical oscillator to its ground state [69].

### 1.3. Sources of Decoherence

Long coherence time is important for coherent control and coupling between spins. However, interactions with the environment and the qubit can result in the destruction of information. The loss of coherence induced on the system, or decoherence, limits the types of interactions and gate operations in QIP.

NV diamonds are no exception to this limitation. The diamond lattice efficiently confines NV centers, which has the advantage of storing information in the nucleus of a neighboring atom [41, 42, 96], but nearby impurities will interact strongly with the defect. More specificially, a large spin-bath creates a perturbative magnetic field

that decreases the spin decoherence time. Additionally, resonant excitation with the excited states offers higher readout of the spin states, adiabatic transfer processes, and strong electron-phonon coupling, but only at the cost of spontaneous emission. This thesis discusses two methods to mitigate decoherence in NV centers and presents preliminary theoretical and experimental work to protect the qubit from decoherence.

Decoherence from interactions with the magnetic environment can be reduced by strongly driving the two-level system. The coherent interaction between the electron spin and radiation field [121] creates superpositions of the spin states, or dressed states, that are separated by an effective Rabi frequency. The separation of these dressed states depends on the Rabi frequency of the driving field and the energy shifts generated by the nuclear spin bath. Stronger driving fields lessen the effect of the magnetic fluctuations, making the dressed states insensitive to perturbations. The dressed states of the NV center have been widely studied using both microwave fields [13, 23, 49, 88, 136, 143, 156, 161] and mechanical motion to dress the ground states [91, 141]. We report preliminary results showing the formation of the dressed states in our system and propose three-level schemes in the NV center that can be used with excited state strain coupling mechanisms.

Stimulated Raman adiabatic passage is a slow and robust way to transfer population between two quantum states via a shared state [46]. Two optical fields are pulsed such that it follows a non-radiative dressed state. But even if the two fields are largely detuned from the transition, the shared state will be populated. Spontaneous emission from the common state causes the collapse of the quantum state which is bad news for quantum information processing. This problem arises from the fields themselves that produce coupling terms between the non-radiative and radiative dressed states. The shortcut-to-adiabaticity (STA) technique is the use

of a third field that cancels out coupling between the dressed states [18, 26, 33]. This method can speed-up the process while maintaining the fidelity of the system. We further explore this technique as it can decrease decoherence from optical pumping in our spin-phonon experiments. Unlike previous experiments that use all optical control to achieve a similar effect [162], our special selection of a Λ-type three-level system lends itself to STA.

### 1.4. Overview of Thesis

Chapter II of this dissertation introduces the nitrogen vacancy center in diamond. It is a brief discussion of the electronic structure and methods to initialize, manipulate, and readout the spin. I provide details on the experimental setup used for the experiments carried out in subsequent chapters.

Chapters III presents my work on coupling NV centers to SAWs. First, I introduce electron-phonon coupling via the excited state in the NV center. I derive a Hamiltonian for the spin-phonon system to find the effective Rabi frequency of the system. Then I provide experimental results on the optomechanical processes. I demonstrate phonon sidebands and Rabi oscillations using a sideband transition. The information presented in Chapter III is previously published material in Physical Review Letters [51] coauthored with Andrew Golter, Thein Oo, Kevin Stewart, and Hailin Wang.

Chapter IV continues with my work on coupling NV centers to SAWs, and focuses on using a phonon-assisted Λ-system to couple SAWs to the spin degrees of freedom of the NV centers via the excited states. This chapter examines the role local strain plays in the structure of the excited state and how it gives rise to non-spin preserving excitations. I study the effects of optical pumping on optically driven

sideband spin transitions. This work was coauthored with Andrew Golter, Thein Oo, Ignas Lekavicius, Kevin Stewart, and Hailin Wang in Physical Review X [50].

Chapter V discusses the use of semi-classical dressed states to suppress effects of spin dephasing. Here I discuss the effects the nuclear spin bath has on the ground states of the NV center and how the dressed states can extend the decoherence time. I perform Mollow Triplet experiments to show the formation of the dressed states. My discussion includes the advantages of using the dressed states for experiments involving mechanical control.

Finally, Chapter VI covers my theoretical calculation on counterdiabatic driving in adiabatic processes and also discusses a proposal for future experiments. This work aims to reduce optically-induced decoherence due to the population of the NV excited states by using counterdiabatic driving. I analyze the causes of non-adiabatic interactions in a three-level systems and probe the parameters necessary to implement a STA scheme in our system.

# CHAPTER II

# NITROGEN VACANCY CENTERS IN DIAMOND: SPIN AND OPTICAL SPECTROSCOPY

## 2.1. Introduction

In recent years, the nitrogen vacancy center in diamond has emerged as a leading quantum bit candidate for quantum computation. This atom-like system exhibits long spin coherences even at room temperature, strong optical transitions that enable all optical control, and coupling to phonons. These features further the development of chip-based diamond technologies which is essential for scalable quantum computing. The first half of this chapter describes the NV centers structure and properties [37, 85, 95] while the latter half presents experimental techniques to probe the spin and optical structure.

## 2.2. Structure of the NV Center

The nitrogen vacancy (NV) center in diamond is a naturally occurring defect in which a substitutional nitrogen atom sits next to a missing carbon atom (see Fig. 2.1). The nitrogen vacancy exists in two charge states [59, 68], the neutral charge state ($NV^0$) and negatively charged state ($NV^-$). The $NV^0$ has five electrons: dangling bonds from the adjacent three carbon atoms contribute one electron each, while the nitrogen atom supplies two valence electrons forming a spin-1/2 system with a zero-phonon line (ZPL) at 575 nm. The $NV^-$ has an extra electron making it a spin-1 system with a ZPL at 637 nm. In this work, we solely investigate the

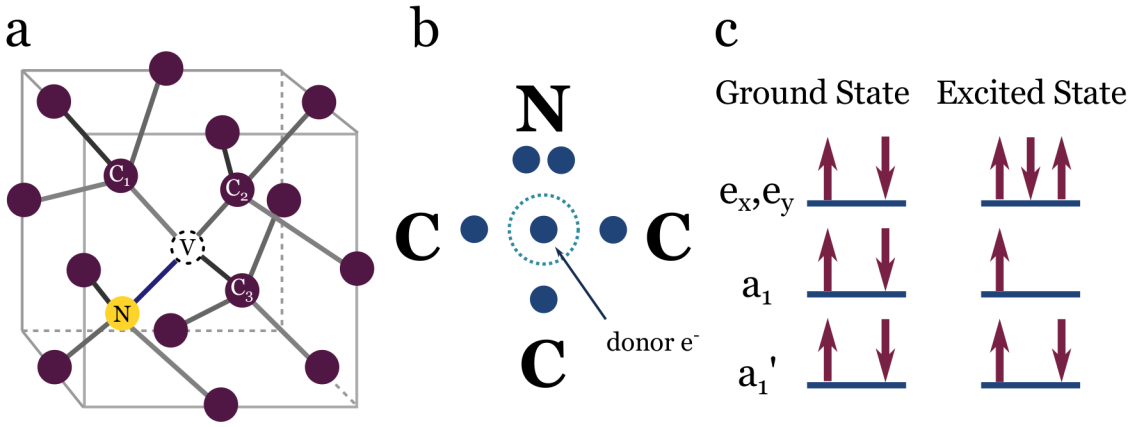


FIGURE 2.1. (a) Diamond lattice with an embedded NV center. Carbon atoms are marked in purple and the nitrogen in yellow. (b) Dot structure of electrons in the vacancy. (c) Electron spin configuration for the ground and excited states.

negatively charged NV center which is commonly found in diamond and simply refer to it as the NV center.

The electron ground state of the NV center is a spin triplet system $^3A_2$ which has been confirmed by numerous magnetic resonance techniques [54, 150]. The $m_s = 0$ state is the lowest energy level split from the $m_s = \pm 1$ states by 2.87 GHz due to electron spin-spin interactions, as illustrated in Fig. 2.2(a). The $m_s = \pm 1$ states can be Zeeman split by adding an external magnetic field oriented along the NV axis, lifting the degeneracy. The nuclear spin from the nearby nitrogen atom, commonly $^{14}$N spin-1 system, couples to the ground states further splitting these states. The $m_s = 0$ state has two hyperfine states corresponding to nuclear spins $m_n = 0, \pm 1$ which are split by 5 MHz due to a quadrupole interaction. The $m_s = \pm 1$ have three hyperfine states split by 2.2 MHz. Studies have also demonstrated nuclear spin coupling to $^{15}$N [44].

The excited state of the NV center exhibits a complex structure which depends on temperature and strain (Fig. 2.2(b)). The excited state of the NV is a spin

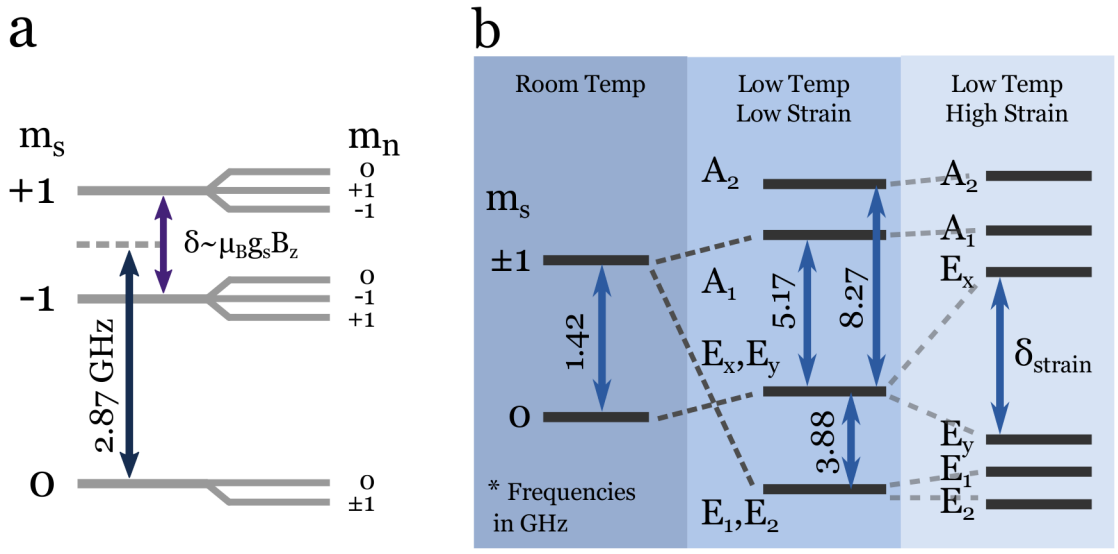


FIGURE 2.2. (a)Ground state structure (b) excited state structure for varying temperature and strain.

triplet orbital doublet system [97, 138], $^3E$, with the $m_s = 0$ excited state 1.42 GHz lower than the $m_s = \pm 1$ states at room temperature. At cryogenic temperatures the excited states split into six levels $\{A_1, A_2, E_x, E_y, E_1, E_2\}$ commonly labelled by their symmetry properties as shown in Fig. 2.3. The spin-orbit interaction produces a 5.5 GHz gap between pairs of states $\{A_1, A_2\}$, $\{E_x, E_y\}$, and $\{E_1, E_2\}$, with the same total angular momentum. The spin-spin coupling parameter shifts $\{E_x, E_y\}$ down by $\approx 0.95$ GHz and $\{A_1, A_2, E_{1,2}\}$ up by $\approx 0.47$ GHz. The spin-spin interaction is also responsible for splitting the $A_1$ and $A_2$ by $\approx 3.3$ GHz. Strain plays an important role in the shifting and mixing of levels which is further discussed in Chapter 4.

Apart from the discrete energy levels, the NV center has a continuum of vibronic energy states which contribute to the absorption and fluorescence spectrum [30]. The former allows efficient initialization using green 532 nm light for room and cold temperature experiments and the latter allows detection at longer wavelengths (650-

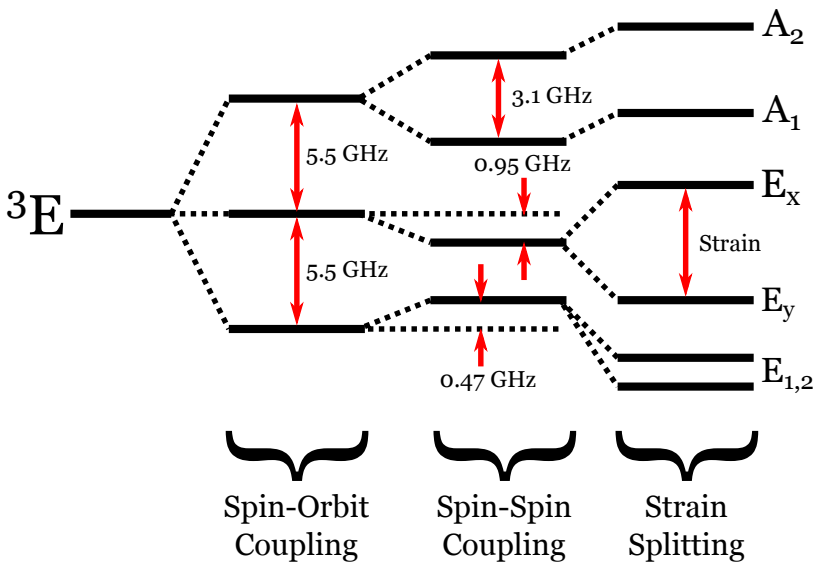


FIGURE 2.3. Excited state energy separation depending on spin-orbit, spin-spin, and strain energy shifts at low temperatures.

800nm). Most of the fluorescence is emitted into the phonon-sideband with only 4% of photons contributing to the ZPL [95].

One special feature of the NV center is its non-radiative pathway which allows optical initialization into the $m_s = 0$ at room temperature and spin-dependent fluorescence. This pair of metastable states exist between the ground and excited states [125], as shown in Fig. 2.4. This allows the population from $m_s = \pm 1$ states to decay into the $m_s = 0$ state and vice versa, although the decay of $m_s = 0$ into $m_s = \pm 1$ is less than 1%. Since the $m_s = \pm 1$ states take this non-radiative path they fluoresce more weakly, thus offering a way to measure the spin state.

## 2.3. Experimental Methods

### 2.3.1. Confocal Microscopy

To study NV centers in diamond we use a home-built low working distance confocal microscope, where the diamond sits in a cryostat for low-temperature

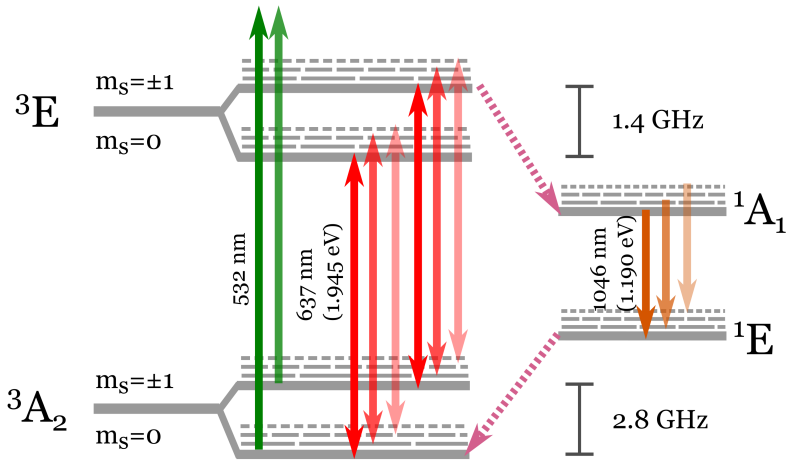


FIGURE 2.4. Energy levels for the NV center at room temperature.

experiments. Our confocal setup includes microwave coupling and magnetic field control. The essential features of our system can be found in Fig. 2.5. We use a type IIa diamond sample for its low nitrogen concentration (∼ppb). Low nitrogen concentrations are necessary for observing coherent processes of the NV spin since this defect couples strongly to nitrogen and single centers are easier to find. All our experiments are done on single NV centers in diamond which we can find by scanning the focal spot of the microscope over a 50 × 50 $\mu$m area. We confirm that they are single NV centers by looking at the resonance fluorescence spectrum. Single centers exhibit narrow linewidths and unique excited energy level splittings.

We optically excite the vibronic sideband using a green 532 nm laser (Laserglow LCS-0532) and perform resonant excitation of the ZPL using a 637 nm tunable diode laser (New Focus, Velocity 6304) and a 637 nm tunable dye laser (Coherent, 899-21). The beams pass through acousto-optic modulators (AOM) with short-rise times to create precise nanosecond pulses. The light is focused onto the sample with a low working distance objective (Nikon CFI Plan LWD IMSI 100x). A set of galvanometers (Thorlabs, GVSM002) steer the focal spot over an area of 50× 50$\mu$ m combined

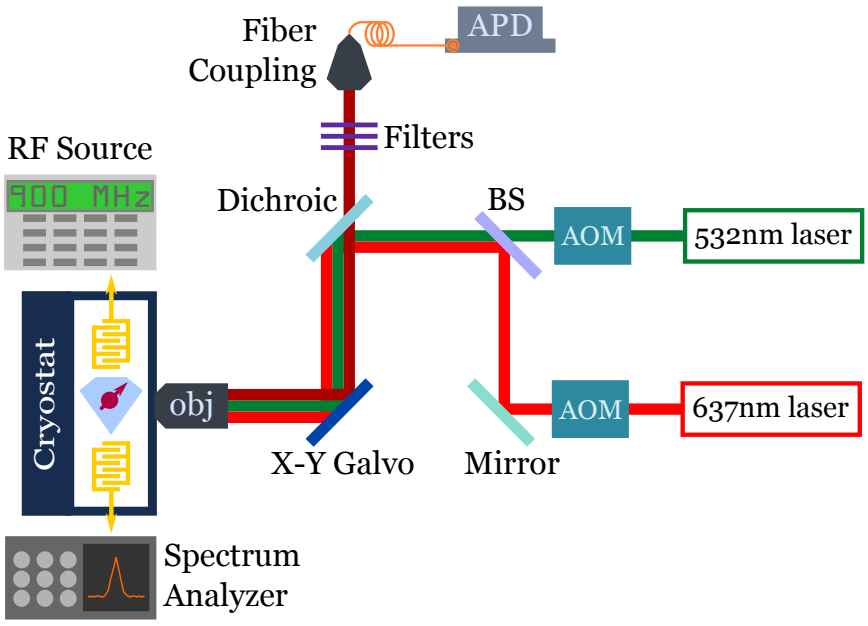


FIGURE 2.5. Confocal setup.

with a piezo-electric actuator (Thorlabs, DRV517) for focus adjustment. Emitted fluorescence from an NV center is collected through the same optical path. A dichroic mirror (long pass 635 nm) and a set of filters (532 nm notch, 638 nm notch, and 650 nm long pass) allow fluorescence from the phonon sideband to be coupled into a fiber. The fiber acts as the pinhole in a typical confocal setup, rejecting light out of the focal plane. The fiber is connected to an avalanche photodiode (Perkin-Elmer, SPCM-AQR-16-FC) for single photon counting using a data acquisition module (National Instruments, PCI 6602).

The SAW experiments require two phase locked fields separated by 2 GHz. Not pictured in Fig. 4 is the double pass set up to achieve this tunable offset. Light from the ring laser is split in two, cross linearly polarized using a half-wave plate and sent through separate AOMs. One beam passes twice through a 1 GHz AOM by using a curved mirror.

To utilize the optical properties of the NV center it must be cooled to cryogenic temperatures. The sample is mounted on a cold finger inside a closed-cycle cryostat (Montana Instruments Cryostation) cooled to 7K. The position of the sample is controlled to sub-nm precision using a 3D stack of piezo stages (Attocube Systems ANP 51 series). We improved the collection efficiency by choosing a low working distance objective paired with a 1 mm thin window with anti-reflective coating on the cryostat window. A magnetic stack sits on a 3-D stage outside of the cryostat to produce Zeeman shifts in the ground state.

A grounded coplanar waveguide (CPW) has been fabricated on top of the diamond. The pattern is made using a laser writing system (MICROTECH) then developed for evaporation. The dimensions and thickness of the metals where chosen to impedance match the 50 Ohm coax cables. We used a 10nm adhesion layer of Ti before depositing 200nm of Al. The CPW is wire bonded to a PCB chip with vacuum compatible wires for sending in an RF signal. In experiments where two fields are required, we use two signal generators and combine the signals using a frequency splitter. A similar process is used for the IDTs and will be discussed in subsequent chapters.

The imaging and data collection is computer controlled using python and LabView. Pulses for experiments are created using a SpinCore card (Pulse Blaster ESR-PRO-400) which generates TTL pulses to synchronize the AOMs, microwave (MW) field, and photon counting.

### 2.3.2. Optical Initialization and Readout

The spin can be readily initialized in the $m_s = 0$ ground state through intermediate states which allow non-spin preserving transitions. A long green pulse

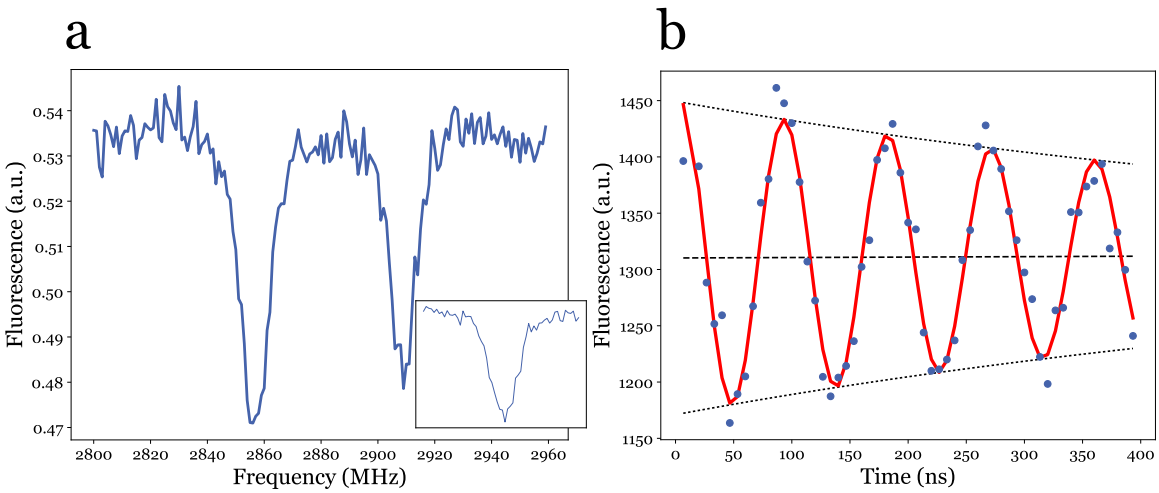


FIGURE 2.6. (a) Fluorescence of a single NV center as a function of microwave frequency with an applied magnetic field. The $m_s = \pm 1$ levels are Zeeman shifted. (inset) Single ODMR dip at 2.87 GHz when no magnetic field is present. (b) Rabi oscillations.

excites all three ground states. The $|0\rangle$ state follows a cycling transition but the $|\pm 1\rangle$ states undergo fewer cycling transitions before decaying through the metastable states into $|0\rangle$. This mechanism enables ground state preparation even at room temperature. Optical readout takes advantage of the same method. If the NV center is in either the $|-1\rangle$ or $|+1\rangle$ state it will emit less photons, displaying a $\sim 20-40\%$ fluorescence contrast compared to $m_s = 0$ ground state [95]. While this preparation and readout process allows us to probe the NV spin at room temperature it limits us to only reading out the population from $|0\rangle$.

### 2.3.3. Optically Detected Magnetic Resonance

The NV center's electron spin can be initialized, with 70% efficiency [64], and measured using optical excitation. The spin can be controlled by applying a MW field tuned to the upper state transition frequencies. This provides the ground work for preparing, manipulating and measuring a single electron spin in diamond.

We use an ODMR continuous-wave measurement as a means to calibrate the microwave frequency required for an excitation. The continuous 532 nm polarizes the NV center into the more fluorescent $m_s = 0$ state; when the microwave field is resonant with either $m_s = -1$ or $m_s = +1$ the population will move into those levels, and the fluorescence decreases. Fluorescence into the phonon sideband is measured as a function of microwave frequency (see Fig. 2.6(a)). The resonance occurs at 2.87 GHz and in the presence of a magnetic field the resonances are shifted by 2.8 MHz/Gauss. The magnetic field strength and orientation determine the magnitude of the Zeeman splitting. When the static magnetic field is aligned with the dipole axis the Zeeman effect is maximized. These ground state transitions have polarization selection rules which are not met for these experiments since the orientation of the CPW determines the polarization. This results in an asymmetry between the two resonance dips.

### 2.3.4. Rabi Oscillations

Pulsed waved experiments allow us to probe the spin dynamics of the system and observe the effects in the time domain. The $m_s = 0$ to $m_s = -1$ transition is used to study the dynamics of a two-level system. Driving this transition with a resonant MW field will induce population transfer from one state to another in a periodic manner; these are known as Rabi oscillations. To observe this effect, we apply a MW pulse with duration $\tau$ and measure the population in $|0\rangle$ as we vary $\tau$. We fit a cosine function to the data to determine the Rabi frequency $\Omega_R$. Fig. 2.6(b) shows a typical oscillation with $\Omega_R$ =10 MHz. We manipulate the Rabi frequency by adjusting the microwave power. The Rabi frequency is used to calibrate the pulse length necessary to flip the spin from $|0\rangle$ to $|-1\rangle$; this is defined as a $\pi$ pulse. The

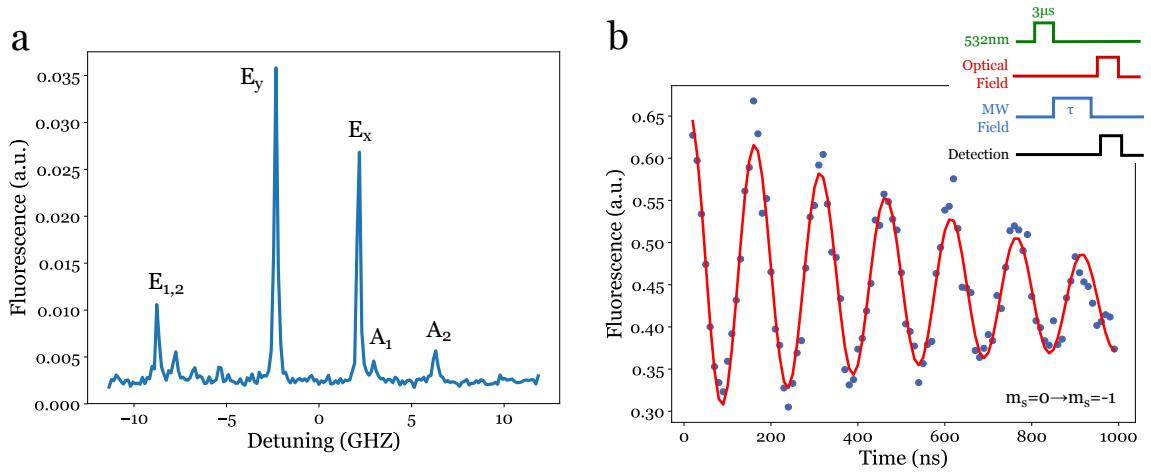


FIGURE 2.7. (a)PLE spectrum for NV. (b) Rabi oscillation experiment with direct optical spin readout. *inset*: Pulse sequence for Rabi oscillation experiment.

hyperfine states have different Rabi frequencies which limit the contrast especially at lower MW powers.

### 2.3.5. Resonant Excitation

At low temperatures the six optical transitions are narrow enough to drive directly [65]. These optical transitions are spin preserving due to angular momentum selection rules [138]. The spin zero excited states $E_{x,y}$ couple to the $m_s = 0$ ground state via linearly polarized light. Non-zero spin states $\{A_1, A_2, E_1, E_2\}$ use circularly polarized light to couple to the $m_s = \pm 1$ ground states. We can precisely measure the spin state $m_s = 0$ by applying an optical field to the spin-cycling transition $E_x$ or $E_y$. This offers higher fidelity since it will not populate the $m_s = \pm 1$ levels as the green would. Additionally we use the $A_2$ excited state to readout population from the $m_s = \pm 1$ states.

The photoluminescence excitation (PLE) spectrum is shown Fig. 2.7(a), revealing the excited state transitions. We scan a laser around 637 nm while collecting the fluorescence from the phonon-sideband. The local strain determines the splitting

of the excited states and is unique to each NV center. In order to see non-zero spin transitions $\{A_1, A_2, E_1, E_2\}$, we apply a continuous MW field that is on resonance with the $m_s = 0$ and $m_s = \pm 1$ transition.

Figure 2.7(b) illustrates the Rabi oscillation experiment between $m_s = 0$ and $m_s = -1$ with direct optical spin readout from the $E_y$ excited state. The inset shows the pulse sequence for the experiment in which we initialize the system with green to prepare the state into $m_s = 0$ and then apply a time varying MW pulse and measure the fluorescence from $m_s = 0$ as a function of the pulse width.

The nitrogen vacancy obtains the sixth electron from nearby electron donors, such as a nearby nitrogen atom. Continuous optical resonant excitation causes the NV center to ionize, converting it to a neutral charge state [45, 94, 123]. The negative charge state can be recovered by off-resonant green excitation, ionizing the nitrogen donor to restore the extra electron of the NV. For this reason we initialize the NV center with a green optical pulse after several optical cycles of resonant excitation.

This chapter provided background information about nitrogen vacancy centers in diamond, which serve as spin system in the subsequent chapters. Microwave and optical manipulation of this system is necessary for understanding and setting up future experiments. The next chapter will focus on strain coupling in the energy levels of the NV center. We will demonstrate coupling between the NV center and an acoustic wave.

# CHAPTER III

# OPTOMECHANICAL QUANTUM CONTROL

This chapter contains previously published material [51]. My main contribution is the theoretical analysis of the experiment. Andrew Golter is responsible for the optical measurements, while Thein Oo fabricated the SAW device and built a real time photon counting device using a field programmable gate array (FPGA). Kevin Steward helped us with the sputtering deposition of zinc oxide on the diamond. My advisor, Hailin Wang oversaw the project and made recommendations.

## 3.1. Introduction

Color centers in diamond, such as NV centers, have emerged as leading qubit candidates for quantum information processing and quantum communication. Their optical and mechanical properties facilitate state preparation, gate operation, and state readout. However, no quantum system is without weaknesses so experimental efforts have focused on the development of hybrid quantum systems. Previous experiments have integrated NV centers in diamond with photons, nearby nuclear spins, and magnetized mechanical resonators. There has also been a strong interest in using phonons (e.g. surface acoustic waves, high overtone bulk acoustic wave) for quantum control and on-chip communication due to experimental successes in trapped ion [84, 103, 158] and cavity optomechanic systems [5, 101].

The field of quantum phononics associated with NV centers has grown exponentially over the last several years due to high-quality factor diamond resonators and piezo-electric microresonators. Phonons present several advantages over photons, such as slower propagation. Device fabrication for acoustic waves is easier than

photonic devices due to longer wavelengths. Phonons are confined to the material since they do not propagate in vacuum, making it easier to guide on chip. Many groups have investigated the effects of strain to the spin triplet ground state [4, 13, 73, 90–92, 112, 140]. Here we present our results on electron-phonon coupling via the excited states of the NV center.

## 3.2. Strain Coupling of a Nitrogen Vacancy Center

The electronic structure of the nitrogen vacancy center can couple to phonons, in particular surface acoustic waves, through its strain properties. Both the ground and excited states experience axial and transverse effects, in which axial strain induces a shift of the crystal-field splitting whereas transverse strain is responsible for state mixing and allowing forbidden transitions.

### 3.2.1. Ground State

Strain in the diamond lattice can be thought of as an effective electric field since strain induced distortions alter the electron density, resulting in a localized electric field. The ground state Hamiltonian in the presence of strain field ($\sigma_{\parallel}$ and $\sigma_{\perp}$) is described by Eq.3.1

$$H_{strain} = \epsilon_{\parallel}\sigma_{\parallel}S_z^2 - \epsilon_{\perp}\sigma_x(S_x^2 - S_y^2) + \epsilon_{\perp}\sigma_y(S_xS_y + S_yS_x) \tag{3.1}$$

where $\epsilon_{\parallel}$ and $\epsilon_{\perp}$ are the strain coupling constants and $S_x$, $S_y$, and $S_z$ are the spin-1 operators. The axial stress $\sigma_{\parallel}$ shifts the $|\pm 1\rangle$ levels from the $|0\rangle$ state. The transverse strain $\sigma_{\perp}$ is responsible for coupling the $|-1\rangle$ and $|+1\rangle$ levels, allowing a dipole-forbidden spin transition. The NV z-axis is along the nitrogen and vacancy, whereas

the x- and y-axis are in the plane of the carbon atoms [35, 97]. Several groups have taken advantage of this mechanically allowed transition to use the $|\pm 1\rangle$ states as the qubit [13, 92]. Many of these experiments have been achieved by focused ion beam milling mechanical resonators out of the diamond [4, 13, 73, 112, 140]. Groups have also demonstrated this work by driving phonons directly with RF devices [90–92]. However, the ground state strain susceptibility ($\sim$ 10 GHz/strain) is several orders of magnitude less than that of the excited state. The low strain susceptibility is attributed to the fact that the ground states of the NV center share the same orbital [16].

### 3.2.2. Excited State

In contrast, the excited state of the NV center exhibits strong electron-phonon coupling due to symmetries in the $e_x$ and $e_y$ orbitals. The strain Hamiltonian for the excited state is of the form

$$H_{strain} = \delta_1(|e_x\rangle\langle e_x| - |e_y\rangle\langle e_y|) + \delta_2(|e_x\rangle\langle e_y| + |e_y\rangle\langle e_x|) \tag{3.2}$$

where $\delta_1$ and $\delta_2$ are different strain parameters describing the shifting and mixing of states [97, 124]. For simplicity, in this chapter we concern ourselves only with shifts between the ground and excited states due to axial strain. We consider the ground state $|g_0\rangle$ interacting with the excited state $|E_y\rangle$ via an acoustic mode and laser field. The Hamiltonian for this system, with the rotating-wave approximation, is given by

$$H = \hbar\omega_m \hat{b^\dagger} \hat{b} + \hbar\omega_0 \sigma^\dagger\sigma + \hbar\frac{\Omega_0}{2}\left[\sigma e^{-i\omega_L t} + h.c.\right] + \hbar g(\hat{b} + \hat{b^\dagger})\sigma^\dagger\sigma \tag{3.3}$$

with $\hat{b^\dagger}, \hat{b}$ denoting the phonon raising and lowering operators with frequency $\omega_m$, whereas $\sigma = |E_y\rangle\langle g_0|$ is the lowering operator of the spin system. The laser field

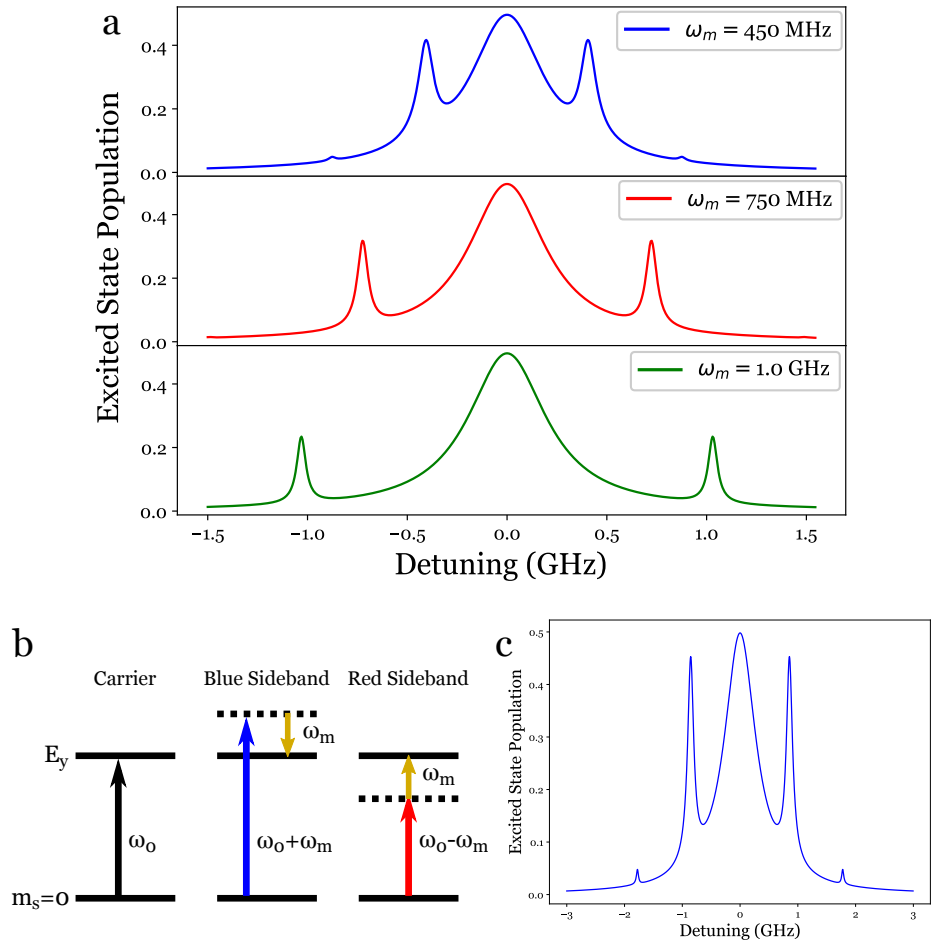


FIGURE 3.1. (a) Simulated excitation spectrum for three different IDT driving frequencies with the same optical Rabi frequency. Sidebands appear at a detuning = $\pm\omega_m$. (b) Energy level diagram for the carrier and sideband transitions. (c) Excitation spectrum with a larger coupling rate than (a). Additional sidebands appear at $\pm 2\omega_m$.

at frequency $\omega_L$ and Rabi frequency $\Omega_0$. The single electron-phonon coupling rate $g = Dk_m\sqrt{\hbar/2m\omega_m}$ depends on the deformation potential $D$, wave number of the acoustic mode $k_m$, and effective mass of the oscillator $m$.

We study the excitation spectrum for a NV center driven at frequency $\omega_m$ by solving the optical Bloch equations for the full Hamiltonian of the system. We plot the excited state population after 80 ns, where the system is in the steady state, as a function of the detuning between the excited state transition frequency and the

optical field. With the acoustic field on, we observe sidebands at $\pm\omega_m$ as shown in Fig. 3.1(a). The Stokes (anti-Stokes) process involves the emission (absorption) of a phonon corresponding to the blue (red) sideband, as illustrated in Fig. 3.1(b). The sidebands increase in amplitude and linewidth for smaller $\omega_m$ because the effects of the direct optical transition are stronger. At larger RF driving powers additional sidebands can be observed (see Fig. 3.1(c)).

To study phonon-assisted sideband transitions we apply the canonical Schrieffer-Wolff transformation,

$$U = exp\left[\eta(b^\dagger - b)\sigma^\dagger\sigma\right] \tag{3.4}$$

where $\eta = \frac{g}{\omega_m}$ is the effective Lamb-Dicke parameter for our system. The Hamiltonian becomes

$$\widetilde{H} = \hbar\omega_m \hat{b^\dagger} b + \hbar(\omega_0 - \eta^2\omega_m)\sigma^\dagger\sigma + \hbar\frac{\Omega_0}{2}[\sigma e^{-i\omega_L t + \eta(\hat{b^\dagger} - \hat{b})} + h.c.] \tag{3.5}$$

which is identical to the trapped-ion Hamiltonian. Transforming into the interaction picture, we get

$$H_I = \hbar\frac{\Omega_0}{2}\left[\sigma e^{-i\delta t} e^{\eta(b^\dagger e^{-i\omega_m t} - be^{i\omega_m t}) + h.c.}\right] \tag{3.6}$$

with $\delta = \omega_L - (\omega_0 - \frac{g^2}{\omega_m})$ as the detuning between the optical dipole transition and the laser field. Then we assume $\eta < 1$ and expand to first order in $\eta$ to get

$$H_I^0 = \hbar\frac{\Omega_0}{2}(\sigma e^{-i\delta t} + h.c.) \tag{3.7}$$

$$H_I^R = \hbar\frac{\Omega_0\eta}{2}(b\sigma^\dagger e^{-i(\delta-\omega_m)t} + b^\dagger\sigma e^{i(\delta-\omega_m)t}) \tag{3.8}$$

$$H_I^B = \hbar\frac{\Omega_0\eta}{2}(b\sigma e^{-i(\delta+\omega_m)t} + b^\dagger\sigma^\dagger e^{i(\delta+\omega_m)t}). \tag{3.9}$$

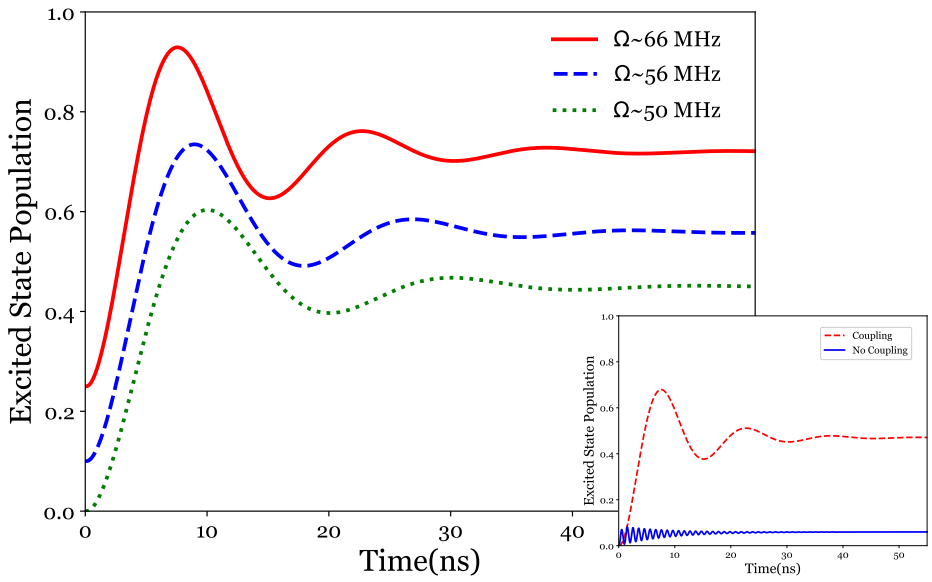


FIGURE 3.2. Calculated optomechanically driven Rabi oscillations for three different RF powers. For clarity, the oscillations displayed are vertically offset. The effective Rabi frequency is indicated in the figure. Inset: Calculated generalized Rabi oscillations (blue curve) using the same parameters, except that the acoustic field is off. For comparison the dashed curve shows the optomechanically driven Rabi oscillation.

The direct optical transition is defined by $H_I^0$ and the red and blue sideband transitions are $H_I^R$ and $H_I^B$, respectively. The effective Rabi frequency of the sideband transition is $\Omega = \sqrt{n}\Omega_0\eta$, where $\sqrt{n}$ is the mean phonon number.

We use Eq. 3.8 to model optomechanically driven Rabi oscillations and discuss contributions from the direct optical dipole transition to the Rabi oscillation experiment. Figure 3.2 shows the Rabi oscillations obtained using the red sideband Hamiltonian with $\Omega_0/2\pi = 290$ MHz and $\omega_m = 940$ MHz. The plot demonstrates Rabi oscillations for different effective Rabi frequencies, which are offset for clarity.The sideband detuned laser field can couple directly to the carrier transition and as a result induce generalized Rabi oscillations of the excited state population. In the inset of Fig. 3.2, we compare the oscillations for the red sideband with the acoustic field on and off, using the same parameters as the $\Omega = 66$ MHz Rabi oscillation. The generalized

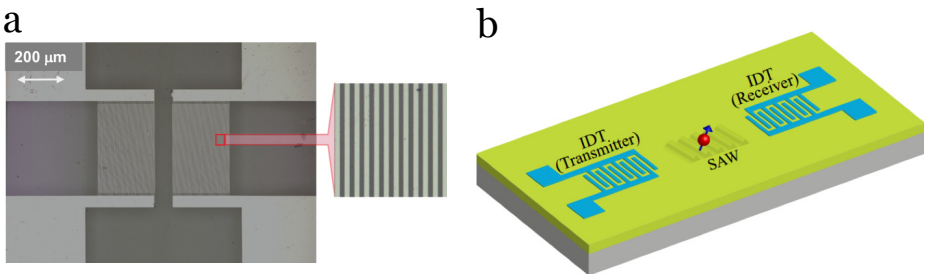


FIGURE 3.3. (a)Two IDT electrodes with wire bonding pads, zoom-ins on IDT fingers. (b)Schematic of diamond sample with IDTs fabricated on the ZnO to drive and detect SAWs.

Rabi oscillations are not observable in our experiments because of the limited time resolution (2.8 ns) of the photon counting module. In this case, the generalized Rabi oscillations lead to a small background contribution to the experiment in Fig. 3.7(b). We also note that in addition to the optomechanically-driven Rabi oscillations due to $H_R$, the combined optical and mechanical coupling can also lead to a weak temporal modulation (with frequency $\omega_m$) in the excited state population. This modulation is not observable in our experiments, again due to the limited time resolution.

### 3.3. Surface Acoustic Waves

Surface acoustic waves (SAW), or Rayleigh waves, propagate along the surface of an elastic solid. SAWs exhibit longitudinal and transverse components. At the surface, these two modes are coupled to each other such that particles travel in an elliptical path. The energy of a SAW is localized within one wavelength into the surface and the amplitude falls off exponentially into the material. The penetration depth of wave into the medium is inversely proportional to its frequency. SAWs can vary from tens of megahertz to several gigahertz.

SAWs can be generated by applying an AC signal to a set of interdigitated electrodes on top of a piezo-electric substrate. The grating like structure is called

an interdigitated transducer (IDT) and converts an electric signal into mechanical motion via the piezoelectric effect. A periodic displacement occurs when a potential is applied across the IDT electrodes. The resonance frequency of the IDT depends on the velocity $v$ of the SAW, which depends on the thickness of the piezo-electric material, and the width $w$ of the electrodes. The wavelength of the SAW is defined as four times the electrode width.

$$f = \frac{v}{4w} \tag{3.10}$$

While diamond has a high elasticity due to its Young Modulus it is not piezoelectric. To create the IDT device we first deposit a layer of zinc oxide (ZnO) and then fabricate the electrodes using electron beam lithography. A detailed explanation of the fabrication process can be found in ref [51, 111]. We made two IDTs, one acts as the transmitter and the second is the receiver, which we connect to a signal analyzer to calibrate the frequency of our device. Using Eq. 3.10, we assume a velocity of 5600 m/s resulting in a frequency of 900 MHz.

### 3.4. Optomechanical Control

In our experiment, we realize optomechanical control of a single NV center through a sideband transition. We also report Rabi oscillations driven by simultaneous optical and mechanical fields. These studies are among the first in coupling NV centers to phonons via the excited state electron-phonon coupling mechanism.

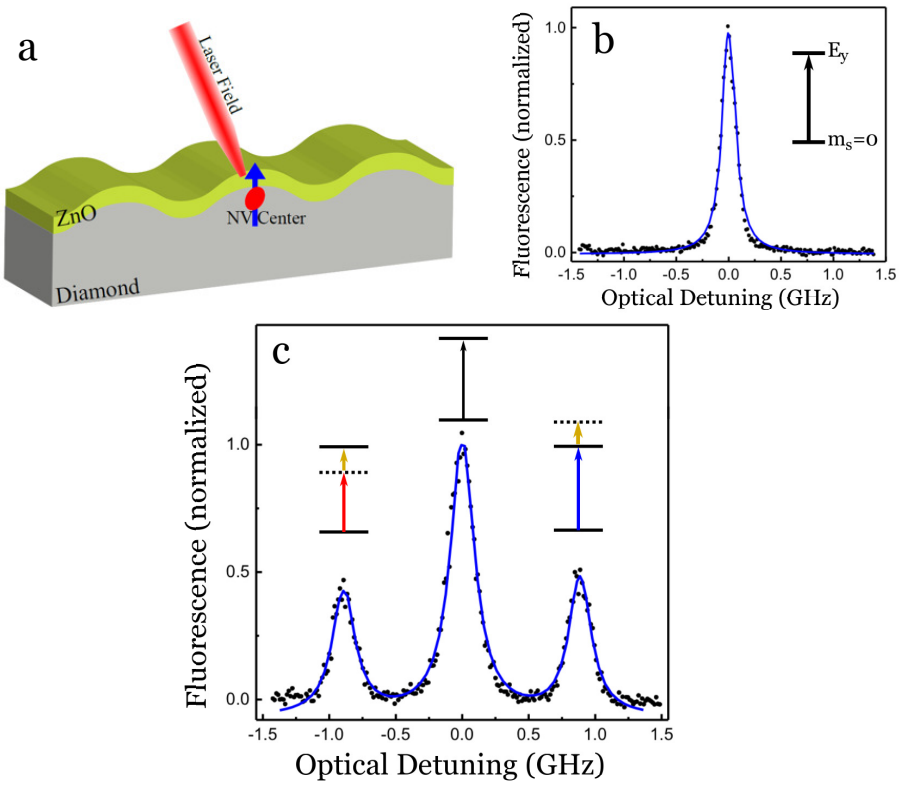


FIGURE 3.4. (a) A NV center near the surface of the diamond couples to a laser field and a propagating SAW that extends from the thin ZnO material to about 6$\mu$m into the diamond. (b) Excitation spectrum of the carrier transition, where the NV fluorescence is measured as a function of the optical detuning. The blue line is a Lorentzian fit. (c)Excitation spectrum with both optical and acoustic fields on and $\omega_m = 900$ MHz. The laser power is $P_0 = 0.4$ $\mu$W and the RF input $P_{RF} = 0.2$ W.

### 3.4.1. Phonon Sidebands

First we probe phonon-assisted optical transitions by considering only strain induced energy shifts of the excited state, as discussed in section 3.2.2. The carrier transition between the $|m_s = 0\rangle$ ground state to $|E_y\rangle$ excited state is used for optomechanical control of the system. The photoluminesence excitation (PLE) spectra is shown in Fig. 3.4(b) with a wavelength near 637 nm. The phonon sidebands can be observed when the the state $|E_y\rangle$ is driven by a laser frequency $\omega_0$ and detuned by the SAW frequency $\pm\omega_m$.

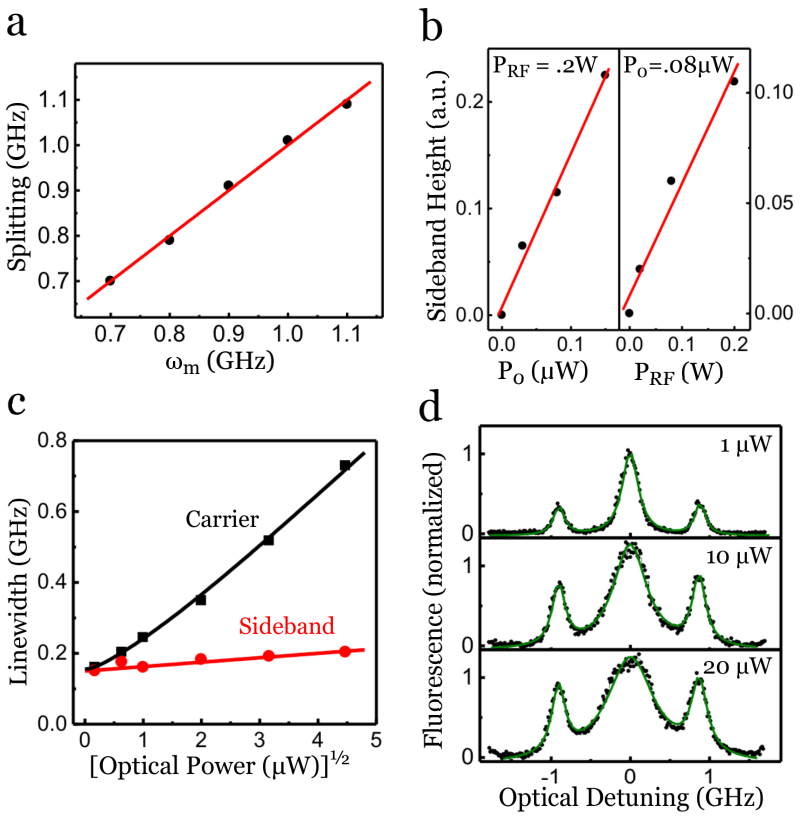


FIGURE 3.5. (a) Measured frequency splitting between the carrier and the sideband transitions as a function of $\omega_m$. The redline is at frequency splitting $= \omega_m$. (b) Amplitudes of the sideband resonances with increasing $P_0$ and $P_{RF}$ powers. Red lines are linear least-squares fits. (c) Linewidths of the carrier (black squares) and sideband (red circles) resonance as a function of $P_0$, with $P_{RF} = 0.2$W. The black line is the calculated power broadening and the red line is a fit to guide the eye. (d) Excitation spectra for the NV center with three different $P_0$ with $P_{RF} = 0.1$W.

We find a single NV center within 2 $\mu$m of the diamond surface such that we can address with optical and surface acoustic fields, see Fig. 3.4(a). The NV is initialized in the $|m_s = 0\rangle$ state, and the fluorescence from $|E_y\rangle$ is measured as a function of the laser detuning from the direct dipole transition. The SAW frequency $\omega_m$ is fixed at 900 MHz. The red and blue sidebands in the PLE spectrum are spectrally separated from the carrier resonance by $\omega_m$ as shown in Fig. 3.4(c). We further verify the sideband transitions are due to acoustic waves by examining the separation

between the central and sideband transitions as a function of the RF frequency of the IDT. Fig. 3.5(a) demonstrates that the splitting is determined by the mechanical driving frequency. The max amplitude of the sideband transitions increases linearly with optical and RF power at relatively low powers for both (Fig. 3.5(b)). We plot the linewidths of the sideband and carrier transitions as a function of the optical power (see Fig. 3.5(c)) noting that the carrier linewidth increases by a factor of 10 compared to the sidebands. The sideband transitions are robust against optical power broadening compared to the carrier resonance, illustrated in Fig. 3.5(d).

The dependence of the carrier resonance linewidth on optical power in Fig. 3.5(c) provides an estimate for the power dependence of the optical Rabi frequency. The linewidth of the NC center optical dipole transition is subject to spectral diffusion due to the off-resonant excitation step in the PLE measurement, as well as to power broadening. The power broadened FWHM, $F_P$, is given by

$$F_P \times 2\pi = 2\gamma\sqrt{1 + \frac{\Omega_0^2}{\gamma\Gamma}} \tag{3.11}$$

where $\gamma$ is the coherence decay rate, and $\Gamma$ is the excited state population decay rate. We treat the spectral diffusion as an inhomogeneous broadening yielding a Gaussian distribution with a linewidth of $F_s$. The convolution of the power broadening and spectral diffusion is a Voigt profile with a FWHM approximated by

$$F \approx 0.535F_P + \sqrt{0.217F_P^2 + F_s^2}. \tag{3.12}$$

We take $\Gamma/2\pi = 14$ MHz and $\gamma/2\pi = 20$ MHz. To fit the data at low optical power we use $F_s = 135$ MHz. To fit the data at the higher power data we take $\Omega_0/2\pi = \sqrt{P_0}\times 65$ MHz, where $P_0$ is the optical power given in units of $\mu$W. The values of $\Omega_0/2\pi$ used

in these experiments are therefore estimated to range between about 10 MHz and 300 MHz. The lack of power broadening for the sideband resonances indicates that under these experimental conditions, $\Omega$ is still small compared with the NV linewidth.

### 3.4.2. Interference Between Carrier and Sideband Transitions

Quantum inference can occur between two different types of excitations from the $m_s = 0$ to $E_y$ states, shown in Fig. 3.6(a). We consider a two-level system with a transition frequency $\omega_0$. There are two complex Rabi frequencies $\Omega_1 = \bar{\Omega_1} e^{-i\omega_1 t + i\phi_1}$ and $\Omega_2 = \bar{\Omega_2} e^{-i\omega_2 t + i\phi_2}$ with $\omega_1$ and $\phi_1$ as the frequency and phase of the carrier transition and $\omega_2$ and $\phi_2$ for the sideband transition. The frequency and phase of the sideband transition incorporate the frequencies and phases of the optical and acoustic fields which drive this transition.

We derive the optical Bloch equations to get

$$\begin{aligned}
\dot{\rho}_{22} &= -\Gamma\rho_{22} + \frac{1}{2}(-i\Omega\rho_{12} + h.c.) && (3.13)\\
\dot{\rho}_{12}^{(1)} &= (-\gamma + i\omega_0)\rho_{12}^{(1)} + i\frac{\Omega_1^*}{2}(\rho_{22} - \rho_{11}) && (3.14)\\
\dot{\rho}_{12}^{(2)} &= (-\gamma + i\omega_0)\rho_{12}^{(2)} + i\frac{\Omega_2^*}{2}(\rho_{22} - \rho_{11}) && (3.15)
\end{aligned}$$

where $\Omega = \Omega_1 + \Omega_2$ and $\rho_{12} = \rho_{12}^1 + \rho_{12}^2$. We take

$$\begin{aligned}
\rho_{12}^{(1)} &= \bar{\rho}_{12}^{(1)} e^{i\omega_1 t}\\
\rho_{12}^{(2)} &= \bar{\rho}_{12}^{(2)} e^{i\omega_2 t} && (3.16)
\end{aligned}$$

and substitute into Eq. 3.14 and Eq. 3.15 to get

$$\begin{aligned}\dot{\bar{\rho}}_{12}^{(1)} &= (-\gamma + i\delta_1)\bar{\rho}_{12}^{1} + i\bar{\Omega}_1 e^{i\phi_1}(\rho_{22} - \rho_{11}) \\ \dot{\bar{\rho}}_{12}^{(2)} &= (-\gamma + i\delta_2)\bar{\rho}_{12}^{2} + i\bar{\Omega}_2 e^{i\phi_2}(\rho_{22} - \rho_{11})\end{aligned} \tag{3.17}$$

where $\delta_{1,2} = \omega_0 - \omega_{1,2}$. Solving these in the steady state gives

$$\begin{aligned}\bar{\rho}_{12}^{(1)} &= -i\frac{\bar{\Omega}_1 e^{i\phi_1}}{2(-\gamma + i\delta_1)} \\ \bar{\rho}_{12}^{(2)} &= -i\frac{\bar{\Omega}_2 e^{i\phi_2}}{2(-\gamma + i\delta_2)}\end{aligned} \tag{3.18}$$

where we take the zeroth order approximation and set $(\rho_{22} - \rho_{11} = -1$.

Next, we combine Eq. 3.16 and Eq. 3.18 and substitute into Eq. 3.13 giving

$$\dot{\rho}_{22} = -\Gamma\rho_{22} + \frac{1}{2}\left[\frac{\bar{\Omega}_1^2}{2(\gamma - i\delta_1)} + \frac{\bar{\Omega}_2^2}{2(\gamma - i\delta_2)} + \frac{\bar{\Omega}_1\bar{\Omega}_2 e^{-i\Delta\omega t}e^{i\Delta\phi}}{2(\gamma - i\delta_2)} + \frac{\bar{\Omega}_1\bar{\Omega}_2 e^{i\Delta\omega t}e^{-i\Delta\phi}}{2(\gamma - i\delta_1)} + c.c.\right] \tag{3.19}$$

where $\Delta\omega = (\omega_1 - \omega_2)$ and $\Delta\phi = (\phi_1 - \phi_2)$.

Now we assume

$$\rho_{22} = \bar{\rho}_{22}^{(0)} + \bar{\rho}_{22}^{(+)}e^{i\Delta\omega t} + \bar{\rho}_{22}^{(-)}e^{-i\Delta\omega t} \tag{3.20}$$

which combined with Eq. 3.19 gives

$$\dot{\bar{\rho}}_{22}^{(0)} = -\Gamma\bar{\rho}_{22}^{(0)} + \frac{1}{2}\left[\frac{\bar{\Omega}_1^2}{2(\gamma - i\delta_1)} + \frac{\bar{\Omega}_2^2}{2(\gamma - i\delta_2)} + c.c.\right] \tag{3.21}$$

$$\dot{\bar{\rho}}_{22}^{(+)} = (-\Gamma - i\Delta\omega)\bar{\rho}_{22}^{(+)} + \frac{1}{2}\left[\frac{\bar{\Omega}_1\bar{\Omega}_2 e^{i\Delta\phi}}{2(\gamma - i\delta_2)} + c.c.\right] \tag{3.22}$$

$$\dot{\bar{\rho}}_{22}^{(-)} = (-\Gamma + i\Delta\omega)\bar{\rho}_{22}^{(-)} + \frac{1}{2}\left[\frac{\bar{\Omega}_1\bar{\Omega}_2 e^{-i\Delta\phi}}{2(\gamma - i\delta_1)} + c.c.\right]. \tag{3.23}$$

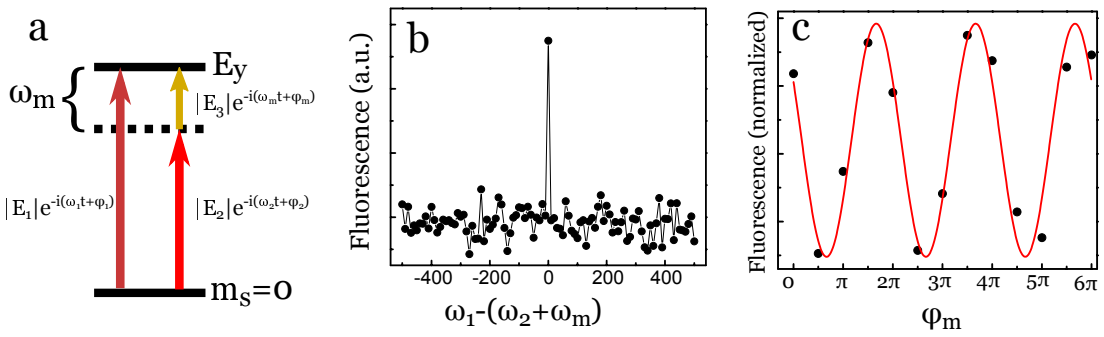


FIGURE 3.6. (a) The arrow on the left indicates the direct optical dipole transition, while the red and yellow arrows on the right are the red sideband transition. (b) NV fluorescence as a function of the frequency different between the three fields. Carrier excitation power is $P_1 = 0.4\mu$W and the optical sideband power is $P_2 = 2\mu$W with $P_{RF} = 0.2W$ for the acoustic wave. (c) Fluorescence of the NV as a function of $\phi_m$ with $\omega_1 - (\omega_2 + \omega_m) = 0$, showing the interference between the two pathways. The red line is a sinusoidal function with a period of $2\pi$.

Solving these in the steady state and substituting back into Eq. 3.20, we arrive at an expression for the excited state population.

$$\begin{aligned}\rho_{22} &= \frac{\bar{\Omega}_1^2}{4(\gamma - i\delta_1)\Gamma} + \frac{\bar{\Omega}_2^2}{4(\gamma - i\delta_2)\Gamma} \\ &+ \frac{\bar{\Omega}_1\bar{\Omega}_2 e^{-i\Delta\omega t}e^{i\Delta\phi}}{4(\gamma - i\delta_2)(\Gamma + i\Delta\omega)} + \frac{\bar{\Omega}_2\bar{\Omega}_1 e^{i\Delta\omega t}e^{-i\Delta\phi}}{4(\gamma - i\delta_1)(\Gamma - i\Delta\omega)} + c.c. \end{aligned} \tag{3.24}$$

Our measurement of the excited state population, by means of the spontaneously emitted fluorescence, averages over a long period of time. This means that when $\Delta\omega$ is nonzero, the phase dependent terms in Eq. 3.24 average to zero. When $\Delta\omega = 0$ the expression simplifies to

$$\rho_{22} = \frac{\bar{\Omega}_1^2 + \bar{\Omega}_2^2}{4(\gamma - i\delta)\Gamma} + \frac{\bar{\Omega}_1\bar{\Omega}_2}{2(\gamma - i\delta)\Gamma}\cos(\Delta\phi) + c.c. \tag{3.25}$$

which has a nonzero phase dependent term that goes as the cosine of the phase difference. Unity contrast in the interference fringes can be achieved if $\Omega_1 = \Omega_2$.

We demonstrate this interference by driving a phonon-assisted optical transition and a direct dipole-optical transition with frequencies $\omega_2 + \omega_m$ and $\omega_1$, respectively. The optical fields are derived from the same laser, maintaining a well-defined relative phase. Furthermore, we lock the phase of acoustic fields to the optical fields. As shown in Fig. 3.6(b), NV fluorescence as a function of $\omega_1 - (\omega_2 + \omega_m)$ exhibits a sharp resonance when the frequency of the optical field for the carrier transition equals that of the sideband transition. The width of the resonance ($< 10$ Hz) is limited by the instrument resolution. Under this resonant condition, we can vary the relative phase of the acoustic field, demonstrating interference between these two transitions as shown by the oscillating NV fluorescence in Fig. 3.6(c). This oscillation shows that the optomechanical processes are fully coherent with the conventional optical processes.

### 3.4.3. Rabi Oscillations

In the resolved sideband regime, we can drive coherent oscillations, or Rabi oscillations, between two levels of an NV center using an acoustic and optical field. The linewidth of the optical dipole transition in our experiment is 200 MHz and the SAW frequency is 900 MHz. Therefore, the optomechanical transition is within the resolved sideband regime. The NV is initially prepared in the $|m_s = 0\rangle$ state and then a continuous optical field is tuned to the red sideband transition. We apply a 90 ns acoustic field while the photon detector is on to detect the fluorescence counts as a function of time, with a bin size of 2.8 ns. As illustrated in the pulse sequence shown in Fig. 3.7(a), we apply the SAW pulse 100 times before initializing the system. Figure 3.7(b) shows the optomechanically driven Rabi oscillations for three different

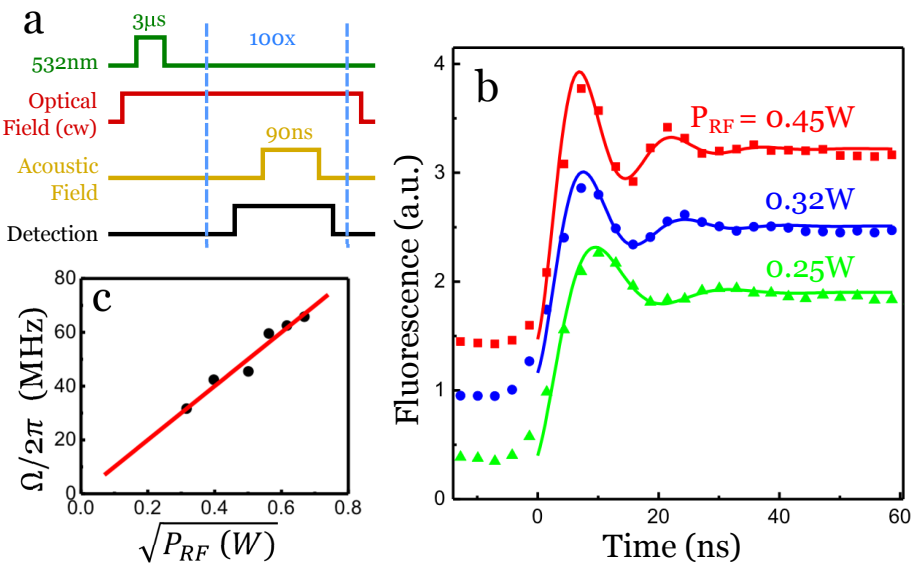


FIGURE 3.7. (a) Pulse sequence used for the Rabi oscillation experiment. (b) NV fluorescence as a function of acoustic pulse duration. Rabi oscillations (offset for clarity) are shown with estimated $\Omega_0/2 = 290$ MHz and for three different RF driving powers for an IDT with $\omega_m = 940$ MHz. Solid lines are numerical fits to damped sinusoidal osillations. (c) Rabi frequencies obtained as a function of the RF power. Ride line shows a linear least-squares fit.

RF driving powers of the IDT. The effective Rabi frequency $\Omega$ increases as the square root of the IDT driving power, see Fig. 3.7(c).

By using the results from the Rabi oscillation experiment we can estimate the amplitude $A_{saw}$ of the surface acoustic waves. The formula is given by

$$A_{saw} = \frac{2}{D}\left(\frac{\omega_m}{k_m}\right)\left(\frac{\Omega}{\Omega_0}\right) \tag{3.26}$$

where D is the deformation potential, $\omega_m/k_m$ is the velocity of the SAW, $\Omega_0$ is the optical Rabi frequency, and $\Omega$ is the effective Rabi frequency. With parameters $D/2\pi = 610$ THz, $\omega_m/k_m = 5600$ m/s, $\Omega_0/2\pi = 290$ MHz and $\Omega/2\pi = 66$ MHz, $A_{saw}$ is approximately 0.7 pm. A small amplitude is required to drive Rabi oscillations because of the strong electron-phonon coupling.

In this chapter, we demonstrated optomechanical quantum control of the energy levels in a NV center by exploiting the strong excited state electron-phonon coupling. These experiments lay down the ground work to couple the spin states of the NV to an acoustic wave. In the next chapter, we use a special $\Lambda$-type three-level system to couple the $m_s = 0$ and $m_s = \pm 1$ states via the excited state $E_y$ through the red sideband and a direct dipole transition.

# CHAPTER IV

# SPIN-PHONON COUPLING OF A NV CENTER

This chapter has been adapted from previously published material with Andrew Golter, Thein Oo, Ignas Lekavicius, Kevin Stewart, and Hailin Wang. It was published in volume 6 issue 4 of Physical Review X in 2016 under the name "Coupling a Surface Acoustic Wave to an Electron Spin in Diamond via a Dark State" [50]. I worked on the theoretical analysis and collaborated with Andrew Golter on studying the effects of optical pumping. Thein Oo fabricated and characterized the interdigitated transducer and collaborated with Andrew Golter and Ignas Lekavicius on the other experiments. Kevin Stewart helped us deposit zinc oxide on the surface of the diamond. Hailin Wang is the principal investigator for this work.

## 4.1. Introduction

Building a quantum phononic network requires robust qubits, such as the spin triplet ground state of the NV center, with strong phonon coupling. However, this presents a technical conundrum. Robust spin qubits necessarily mean extremely weak coupling to acoustic vibrations [36, 97] since otherwise the coupling would lead to a rapid decay of the spin coherence. The ground state is largely unaffected by strain due to the antisymmetric combination of the $e_x$ and $e_y$ orbitals, however, the symmetric orbital configuration of the excited state make it highly susceptible to lattice distortions [15, 36, 97]. Previously, we demonstrated how an electron spin associated with a diamond defect couples to a surface acoustic wave via the excited state electron-phonon coupling mechanism [51]. The excited state is limited by spontaneous emission and spectral diffusion, making it unsuitable for defining the

qubit states. We can overcome this dilemma by coupling a SAW to the electron spin through an optically prepared dark state. In this chapter, we present a scheme to couple the electron spin to a SAW via a Λ-type three-level system where two spin ground states couple to a common excited state via a phonon-assisted sideband transition and a direct dipole optical transition. This method uses the excited state to mediate the phonon interaction without populating the excited state due to an adiabatic elimination.

## 4.2. The Dark State

The Λ-system can be formed with two ground states $|g_1\rangle$, $|g_2\rangle$ and a shared excited state $|e\rangle$ (See Fig. 4.1(a)) in the NV center in diamond [49, 52]. The interaction Hamiltonian for this three level system is given by Eq. 4.1,

$$H_I^0 = \hbar\frac{\Omega_1}{2}(e^{-i\Delta_1 t}|g_1\rangle\langle e| + h.c.) + \hbar\frac{\Omega_2}{2}(e^{-i\Delta_2 t}|g_2\rangle\langle e| + h.c.) \tag{4.1}$$

where $\Delta_1$ and $\Delta_2$ are the detuning of the laser fields from the direct dipole transition frequency, with Rabi frequency $\Omega_1$ ($\Omega_2$) for the $|g_1\rangle \rightarrow |e\rangle$ ($|g_2\rangle \rightarrow |e\rangle$) transition. The instantaneous eigenstates of the system are:

$$|B_+\rangle = \sin\theta\sin\phi|g_1\rangle + \cos\theta\sin\phi|g_2\rangle + \cos\phi|e\rangle \tag{4.2}$$

$$|B_-\rangle = \sin\theta\cos\phi|g_1\rangle + \cos\theta\cos\phi|g_2\rangle - \sin\phi|e\rangle \tag{4.3}$$

$$|D\rangle = \cos\theta|g_1\rangle - \sin\theta|g_2\rangle \tag{4.4}$$

with eigenenergies $E_+ = \hbar\Omega\cot\phi/2$, $E_- = \hbar\Omega\tan\phi/2$, and $E_d = 0$. The effective Rabi frequency is defined as $\Omega = \sqrt{\Omega_1^2 + \Omega_2^2}$, and the mixing angles $\theta$ and $\phi$ are, respectively, $\tan\theta = \frac{\Omega_1}{\Omega_2}$ and $\tan 2\phi = \frac{\Omega}{\Delta}$. Note the Raman resonant condition is

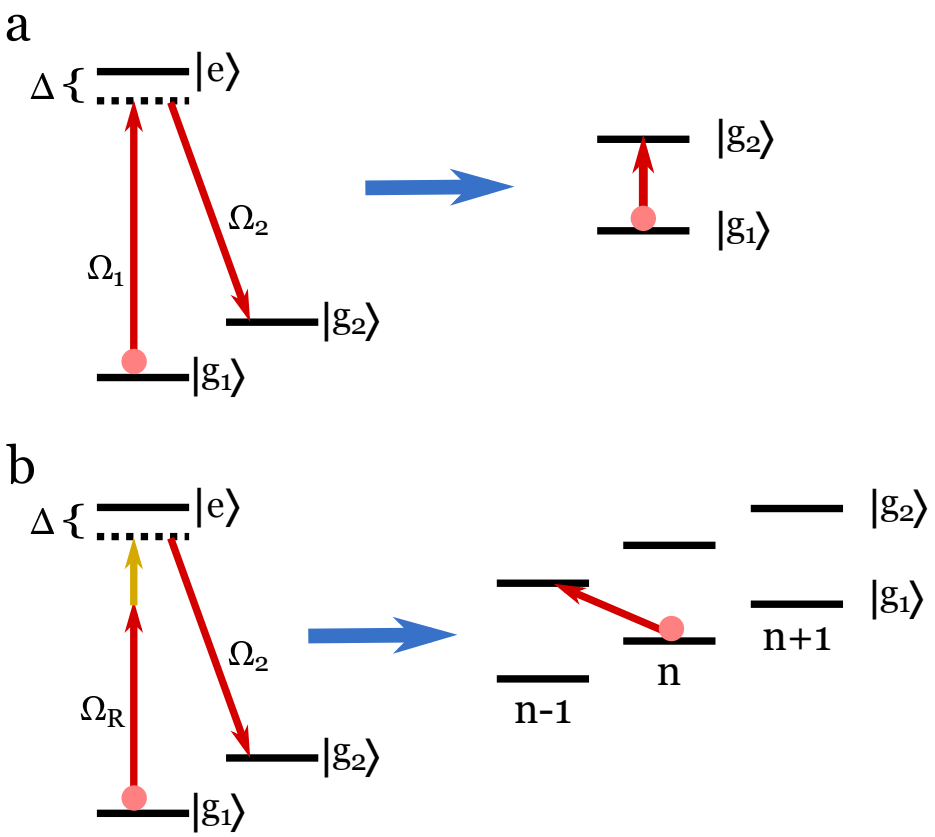


FIGURE 4.1. (a) Schematic of a Λ-type three level system driven by two optical fields with Rabi frequency $\Omega_1$ and $\Omega_2$. In the limit of large dipole detuning, $\Delta$, the system becomes equivalent to an optical transition between the two lower states. (b) Schematic of Λ-system driven by an acoustic field (yellow line) as well as two optical fields. The $|g_1\rangle$ to $|e\rangle$ transition is a red phonon sideband transition with effective Rabi frequency, $\Omega_R$. For large $\Delta$, the system becomes equivalent to an optically driven transition between phonon ladders of the two lower states, where $n$ denotes the phonon number.

$\Delta_1 = \Delta_2 = \Delta$. The dark state, given by Eq. 4.4, is a coherent superposition state of the two lower states, decoupled from the upper state. This transfer from $|g_1\rangle \rightarrow |g_2\rangle$ is realized via the dark state.

In this system, we want the two spins states to couple to the SAW which we achieve by replacing one of the direct dipole optical transitions with a phonon-assisted optical transition, the red sideband transition in this case, as shown in Fig. 4.1(b).

The Hamiltonian, with the rotating wave approximation, is given by

$$\begin{aligned} H &= \hbar\omega_m b^\dagger b - \hbar\nu_1|g_1\rangle\langle g_1| - \hbar\nu_2|g_2\rangle\langle g_2| + \hbar g(b^\dagger + b)|e\rangle\langle e| \\ &+ \hbar\frac{\Omega_1}{2}(e^{i\omega_1 t}|g_1\rangle\langle e| + h.c.) + \hbar\frac{\Omega_2}{2}(e^{i\omega_2 t}|g_2\rangle\langle e| + h.c.). \end{aligned} \tag{4.5}$$

Using the techniques from the previous chapter, we apply the Schrieffer-Wolff transformation and expand the mechanical displacement to linear order to study the dynamics. The Hamiltonian becomes

$$\begin{aligned} \tilde{H} &= \hbar\omega_m b^\dagger b - \hbar\nu_1|g_1\rangle\langle g_1| - \hbar\nu_2|g_2\rangle\langle g_2| + \hbar\eta^2\omega_m|e\rangle\langle e| \\ &+ \hbar\frac{\Omega_1}{2}(e^{i\omega_1 t+\eta(b^\dagger - b)}|g_1\rangle\langle e| + h.c.) + \hbar\frac{\Omega_2}{2}(e^{i\omega_2 t+\eta(b^\dagger - b)}|g_2\rangle\langle e| + h.c.) \end{aligned} \tag{4.6}$$

where $\eta = g/\omega_m$ is effective the Lamb-Dicke parameter. Transforming to an interaction picture, we then have

$$\begin{aligned} \tilde{H}_I &= \hbar\frac{\Omega_1}{2}(e^{-i\tilde{\Delta}_1 t}e^{\eta(b^\dagger e^{i\omega_m t} - be^{-i\omega_m t})}|g_1\rangle\langle e| + h.c.) \\ &+ \hbar\frac{\Omega_2}{2}(e^{-i\tilde{\Delta}_2 t}e^{\eta(b^\dagger e^{i\omega_m t} - be^{-i\omega_m t})}|g_2\rangle\langle e| + h.c.) \end{aligned} \tag{4.7}$$

where $\tilde{\Delta}_1 = (\nu_1 - g^2/\omega_m) - \omega_1$ and $\tilde{\Delta}_2 = (\nu_2 - g^2/\omega_m) - \omega_2$ are the effective detunings. We tune the $\Omega_1$ field near the red sideband of the $|g_1\rangle$ to $|e\rangle$ transition ($\tilde{\Delta}_1 \approx \omega_m$) and the $\Omega_2$ field is near the $|g_2\rangle$ to $|e\rangle$ transition ($\tilde{\Delta}_2 = 0$). Expanding $\tilde{H}_I$ to first order in $\eta$ and keeping only resonant terms, we can approximate the interaction Hamiltonian as

$$H_I = \hbar\frac{\Omega_1\eta}{2}(b^\dagger e^{-i\Delta_R t}|g_1\rangle\langle e| + h.c.) + \hbar\frac{\Omega_2\eta}{2}(b^\dagger e^{-i\Delta_2 t}|g_1\rangle\langle e| + h.c.) \tag{4.8}$$

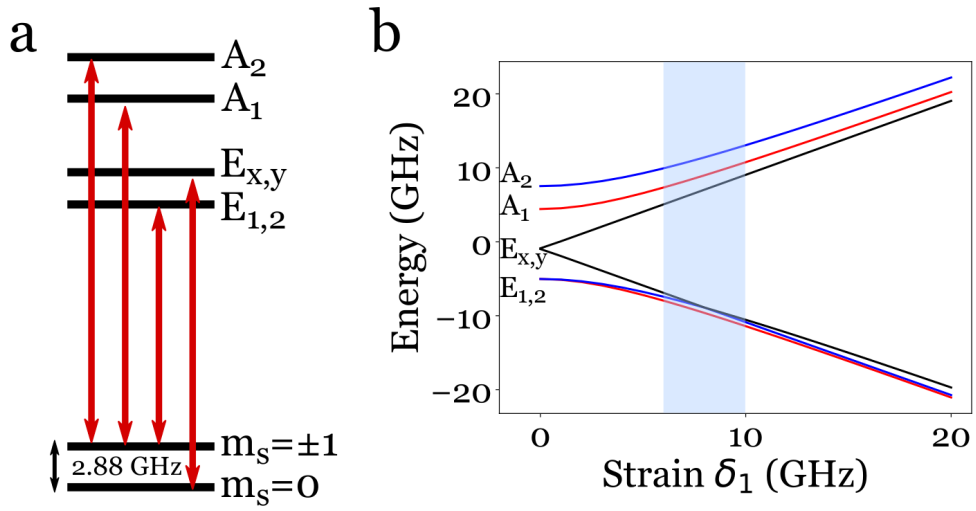


FIGURE 4.2. (a) Energy-level structure and dipole optical transitions of a NV center (without strain). (b) Excited state energies as a function of the strain parameter $\delta_1$.

with $\Delta_R = \Delta_1 - \omega_m$. The effective Rabi frequency for the red sideband is $\Omega_R = \sqrt{n}\Omega_1\eta$. The Hamiltonian in Eq. 4.8 is also valid for relatively large $\Delta_R$ and $\Delta_2$, as long as $\Delta_R \approx \Delta_2$. The dark state for this system, with $\Delta_R = \Delta_2$, is

$$|D\rangle = \frac{1}{\sqrt{\Omega_R^2 + \Omega_2^2}}(\Omega_R|g_2\rangle - \Omega_2|g_1\rangle). \tag{4.9}$$

This dark state can mediate and control the interaction between the spin states and the relevant phonon mode.

### 4.3. Excited State Spin Mixing

As discussed in Chapter 2, the electronic energy level structure of a NV center features a spin triplet ground state $\{m_s = 0, \pm 1\}$ and a spin triplet orbital doublet excited state $\{A_{1,2}, E_{x,y}, E_{1,2}\}$. At low strain, dipole optical transitions occur between the $m_s = 0$ and $E_{x,y}$ states and between $m_s = \pm 1$ and $A_{1,2}, E_{1,2}$, as illustrated in Fig. 4.2(a). A $\Lambda$-type three-level system can be formed with $m_s = \pm 1$ as the lower states

and $A_2$ as the upper state. States $A_1$ and $E_{1,2}$ can also be serve as the upper state in the $\Lambda$-system but are not ideal because of state mixing mechanisms and they largely decay non-radiatively. This $\Lambda$-system presents a technical dilemma: it is implemented using microwave fields. For our experiments, instead we exploit the strain properties associated with the excited states to elect a $\Lambda$-system that has efficient optical spin detection and can be implemented without the use of microwave fields.

Local strain in the diamond splits the degeneracy between the $e_x$ and $e_y$ orbitals in the excited state configuration and results in their mixing. The strain Hamiltonian is governed by two different parameters $\delta_1$ and $\delta_2$ describing lattice distortions. In the high strain regime, spin mixing allows non-preserving spin transitions via linearly polarized light. The full Hamiltonian for the excited state energy levels is

$$H_{Excited} = H_{spin-spin} + H_{spin-orbit} + H_{strain} \tag{4.10}$$

which can be written in matrix form with basis states $\{|A_1\rangle, |A_2\rangle, |E_x\rangle, |E_y\rangle, |E_1\rangle, |E_2\rangle\}$ as [97]

$$H = \begin{pmatrix} \Delta - \Delta^{'} + \lambda_z & 0 & 0 & 0 & \delta_1 & -i\delta_2 \\ 0 & \Delta + \Delta^{'} + \lambda_z & 0 & 0 & i\delta_2 & -\delta_1 \\ 0 & 0 & -2\Delta + \delta_1 & \delta_2 & 0 & i\Delta^{''} \\ 0 & 0 & \delta_2 & -2\Delta - \delta_1 & \Delta^{''} & 0 \\ \delta_1 & -i\delta_2 & 0 & \Delta^{''} & \Delta - \lambda_z & 0 \\ i\delta_2 & -\delta_1 & -i\Delta^{''} & 0 & 0 & \Delta - \lambda_z \end{pmatrix} \tag{4.11}$$

where $\lambda_z = 5.3$ GHz is the axial spin-orbit interaction [14]. The spin-spin induced zero-field splittings are defined by $3\Delta \approx 1.42$ GHz and $\Delta^{'} \approx 1.55$ GHz. The spin-spin

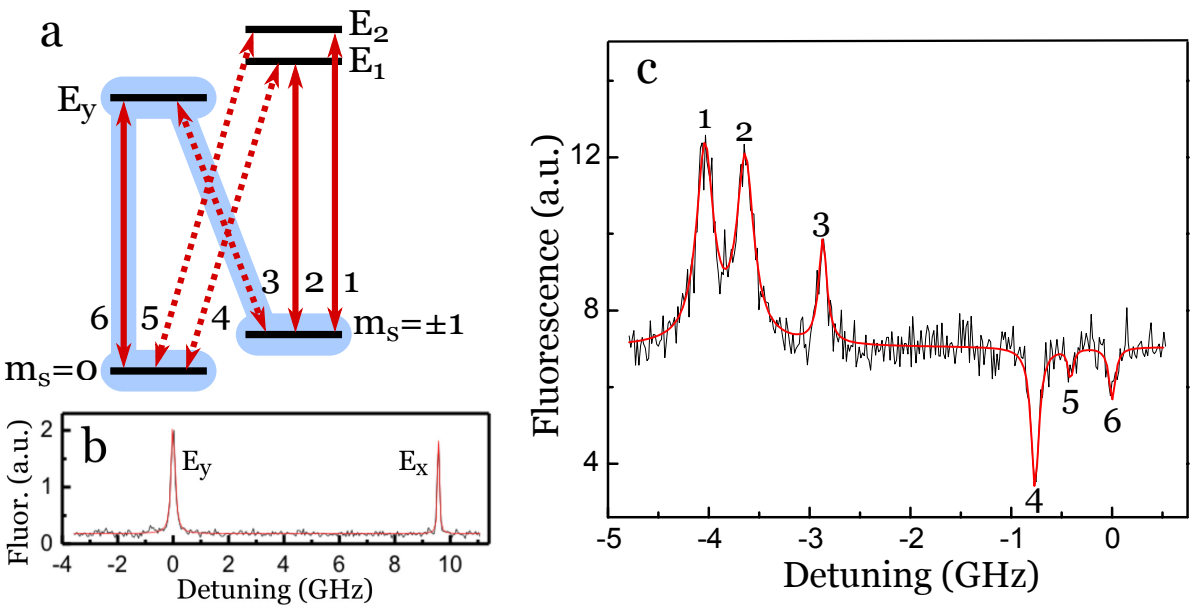


FIGURE 4.3. (a) State mixing due to built-in dc strain, leading to additional dipole transitions, as indicated by the dashed lines. Shaded levels and arrows highlight the Λ-type three level system used in our experiments. (b) Excitation spectrum obtained with no pump field. (c) Excitation spectrum with a pump field fixed at the $E_x$ transition. Peak labels indicate the corresponding transitions labeled in (a).

interaction term $\Delta'' \approx 0.2$ GHz is responsible for mixing states with different spin projections [129]. Previous experiments demonstrated spin-flip optical transitions in a low strain environment [14, 43, 128, 129, 138], although, the spin-flip was originally attributed to the non-axial spin-orbit interaction [95]. Using the Hamilonian above (Eq. 4.11), we solve for eigenenergies and plot them as a function of strain parameter $\delta_1$, as shown in Fig. 4.2(b). The mixing becomes important for $6 < \delta_1 < 10$ GHz, corresponding to an anti-crossing between $|E_y\rangle$ and $|E_{1,2}\rangle$, allowing spin-flip optical transitions. As shown in Fig. 4.3(a), a Λ-type three-level system can be formed with $|E_y\rangle$ as the shared upper state for $|m_s = 0\rangle$ and $|m_s = \pm 1\rangle$ as the lower states.

Our scheme does not require microwave control so we carried out detailed photoluminescence excitation (PLE) experiments to characterize the optical selection rules. The PLE spectrum in Fig. 4.3(b) shows the fluorescence from a single NV

center as a function of a probe laser field near $\lambda \sim 637$ nm. The pronounced peaks are the $E_x$ and $E_y$ resonances with a splitting of 9.6 GHz, indicating a large dc strain. These conditions meet the necessary requirements for state mixing to occur, allowing spin-flip optical transitions for our desired $\Lambda$-system. To find the resonance frequencies for the $m_s = \pm 1$ states, we applied a second pump laser, resonant with $m_s = 0 \rightarrow E_x$ and measured the fluorescence as a function of the probe frequency. The pump probe excitation spectrum (see Fig. 4.3(c)) features three peaks, from the $m_s = \pm 1$ states, and three dips, from the $m_s = 0$ state. The probe excitations from $m_s = \pm 1$ pump the electron spin back into $m_s = 0$ increasing the fluorescence. In contrast, the $m_s = 0$ probe excitations pump the NV into the $m_s = \pm 1$ states, reducing the fluorescence from the pump-driven $E_x$ transition.

The fluorescence background in the PLE spectrum is due to the pump-driven $E_x$ excitation. This transition can also pump the electron spin to the $m_s = \pm 1$ ground states since $E_x$ has a small probability of decaying to the $m_s = \pm 1$ states. The pump-probe experiment is also sensitive to the underlying optical pumping process of the probe.

## 4.4. Three-Level Lambda System Experiments

### 4.4.1. Phonon-Assisted Coherent Population Trapping

As mentioned in the previous chapter, the SAWs with frequency $\omega_m$ are generated by fabricating a pair of interdigitated transducers (IDTs). For the $\Lambda$-system, light from a frequency stabilized tunable dye laser is split into two beams. The detuning between the two laser fields is set by the two acousto-optic modulators (AOMs). One field with frequency $\omega_0$ drives the red-sideband excitation for the $|m_s = 0\rangle$ to $|E_y\rangle$ transition and the other field with frequency $\omega_\pm$ drives the direct dipole transition

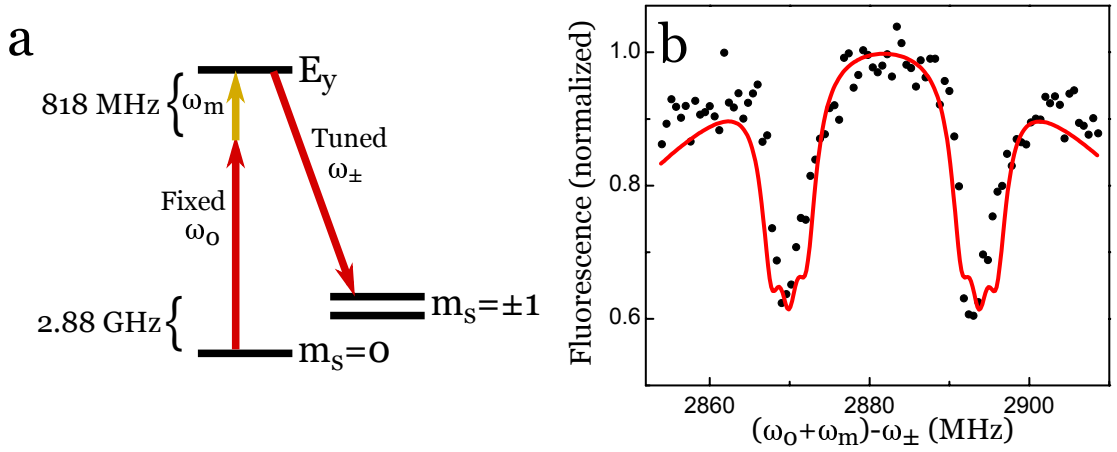


FIGURE 4.4. (a) Energy level diagram used for phonon-assisted CPT experiment. Solid red arrows are the optical fields and the yellow arrow is the acoustic field. (b) Fluorescence of the excited state $E_y$ as a function of $(\omega_0 + \omega_m) - \omega_\pm$. The optical power at frequency $\omega_0$ ($\omega_\pm$) is 4 $\mu$W (1 $\mu$W). The RF input power for the IDT is 0.13 W. The two dips correspond to $\Lambda$-type systems formed with either the $m_s = +1$ or the $m_s = -1$ state. The solid red curve is the theoretical calculation. The fluorescence is normalized to the peak of the theoretical excitation spectrum with no CPT.

between the $|E_y\rangle$ and $|m_s = \pm 1\rangle$ states, as indicated in Fig. 4.4(a). A small magnetic field is applied, resulting in a Zeeman splitting of $\omega_B/2\pi = 24$ MHz between the $m_s = \pm 1$ ground states. First, we observe coherent population trapping (CPT) from the coherent coupling between a SAW ($\omega_m = 818$ MHz) and an electron spin via the dark state, as defined in Eq. 4.9. When pumped into the dark state, a NV center will remain trapped in the dark state, thus quenching the NV fluorescence. Figure 4.4(b) shows the excited state fluorescence as a function of the detuning $(\omega_0 + \omega_m) - \omega_\pm$ between the two arms of the $\Lambda$-system. Two CPT dips are observed in Fig. 4.4(b) because two phonon-assisted $\Lambda$-type three-level systems are involved in this case: $\{m_s = 0, m_s = -1, E_y\}$ and $\{m_s = 0, m_s = +1, E_y\}$. The dips occur when the Raman resonant condition is met, i.e., when the detuning is equal to the frequency separation between the lower states. The solid line in Fig. 4.4(b) is a model of the phonon-assisted CPT experiment using the density matrix equations derived from

the Hamiltonian in Eq. 4.8. There is general agreement between the theory and the experiment, except our model exhibits the hyperfine splitting from the nitrogen atom with nuclear spin $I = 1$. These hyperfine states cannot be resolved in our experiments because of power broadening and limited signal-to-noise ratio. Assuming $\Omega_R = \Omega_\pm$, the observed depth of the CPT dip yields $\Omega_R = 8$ MHz, in agreement with the Rabi frequency estimated from the individual dipole optical or phonon-assisted optical transitions.

### 4.4.2. Optically Driven Sideband Transitions

We carry out spectral-domain experiments to demonstrate the sideband spin transitions via the phonon-assisted $\Lambda$-type three-level system. Figure 4.5(a) illustrates our experimental scheme with a direct spin detection, by exciting the electron spin from $m_s = \pm 1$ to $A_2$ and measuring the corresponding fluorescence. After the NV center is initialized into the $m_s = 0$ ground state, two optical fields are applied with duration 2 $\mu$s, as indicated in Fig 4.5(b). The SAW field was kept on continuously because it only contributes when the corresponding optical field is on. The population of the $m_s = \pm 1$ states is detected after the optical driving pulses. Figure 4.5(c) plots the fluorescence from $A_2$ versus the detuning $(\omega_0 + \omega_m) - \omega_\pm$, with fixed $\omega_0$ and $\omega_m$. The sideband spin transitions occur when the Raman resonant condition is met. The spectral linewidth of the transitions is 0.7 MHz, which is in accordance to the spin dephasing rate. The hyperfine structure of the nitrogen atom is clearly resolved, with a 2.2 MHz splitting. This demonstrates that the sideband spin transitions are nuclear-spin dependent, thus allowing the use of nuclear spin in quantum acoustics.

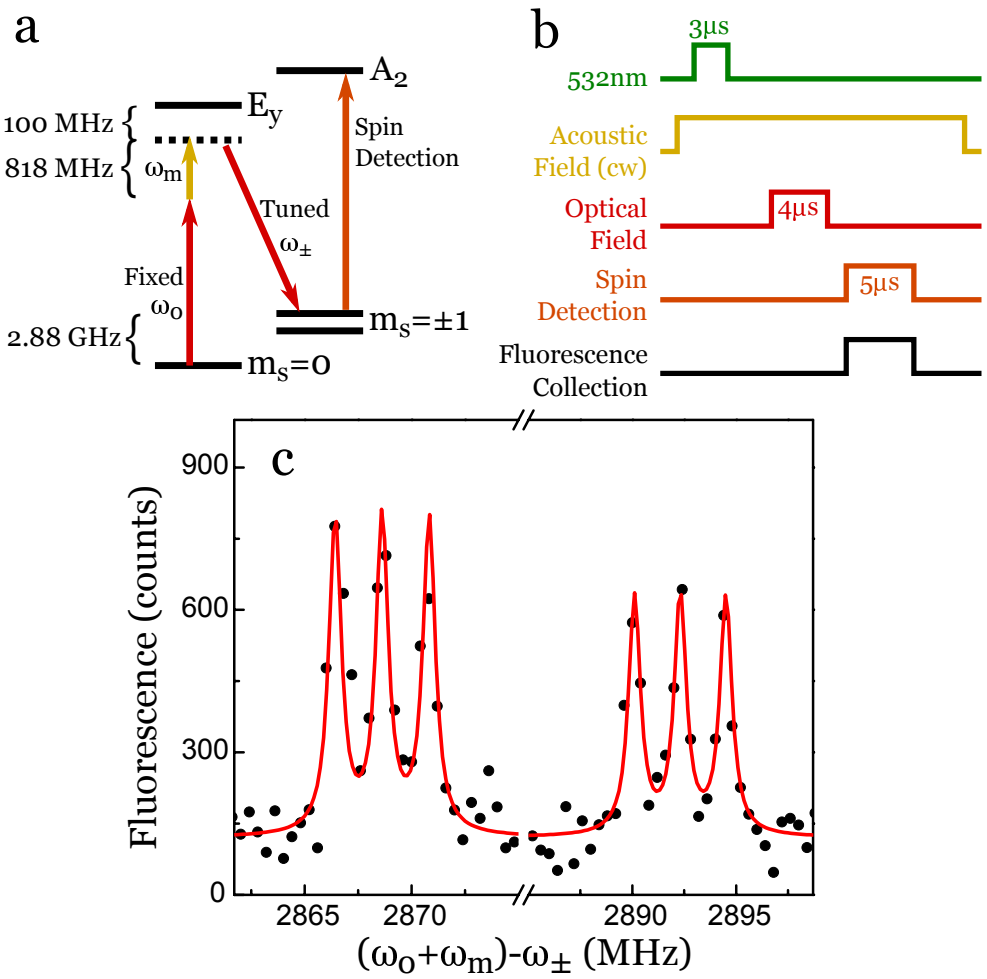


FIGURE 4.5. (a) Energy level diagram including spin detection used for the sideband spin transition experiments. (b) Pulse sequence used for the spectral-domain experiment. (c) Fluorescence from state $A_2$ as a function of $\omega_0 + \omega_m - \omega_\pm$. The solid red line is a fit to six Lorentzians with equal linewidths. A background due to the optical pumping has been subtracted from the data.

### 4.4.3. Effects of Optical Pumping

We have shown CPT between a SAW and the electronic spin associated with an NV center by using a phonon-assisted Λ-scheme, however, excitation of the short-lived excited state induces optical decoherence into the system. In 1990, Gaubatz et al. [47] proposed stimulated Raman adiabatic passage (STIRAP) as a method to efficiently and selectively transfer population between two states without suffering

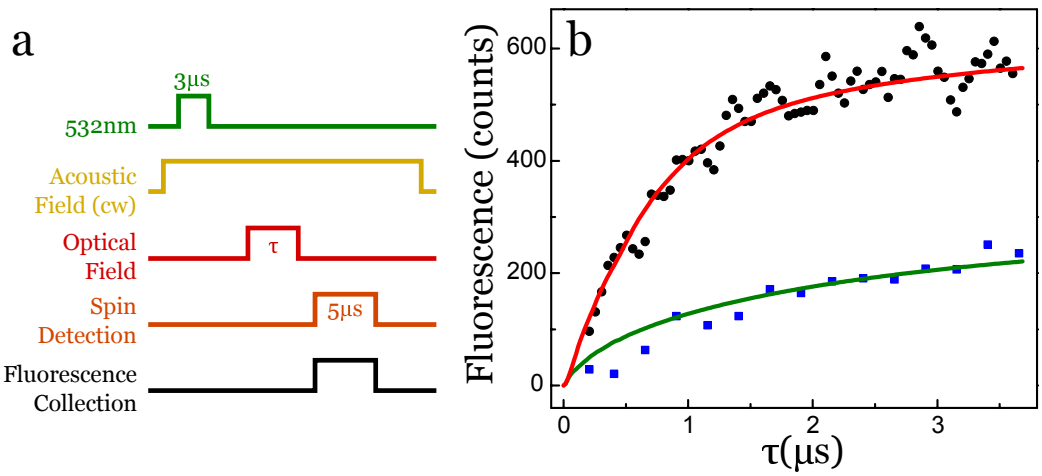


FIGURE 4.6. (a) Pulse sequence used for the transient sideband spin transition experiment. (b) Fluorescence from the state $A_2$ as a function of the optical pulse duration. Solid circles: $\omega_0 + \omega_m - \omega_\pm$ satisfies the Raman resonant condition for the sideband spin transition. Solid squares: $\omega_0 + \omega_m - \omega_\pm$ is 6.5 MHz detuned from the Raman resonant condition (the data are smoothed). The solid lines are the theoretical calculations.

loss to spontaneous emission. The dynamics of the upper state in the Λ-system can be adiabatically eliminated if the fields are sufficiently detuned from the respective dipole transitions. Under this condition, the system becomes an effective two level system with an effective Rabi frequency

$$\Omega_{STIRAP} = \frac{\Omega_1 \Omega_2}{2|\Delta|} \tag{4.12}$$

where $\Omega_1$ and $\Omega_2$ are the Rabi frequencies of the optical transitions and $\Delta$ is the dipole detuning. For our system, we replace $\Omega_1$ and $\Omega_2$ with the red-sideband Rabi frequency $\Omega_R$ and the $m_s = \pm 1$ Rabi frequency $\Omega_\pm$ to obtain an effective Rabi frequency of

$$\Omega_{SS} = \frac{\Omega_R \Omega_\pm}{2|\Delta|} = \frac{\Omega_0 \Omega_\pm}{2|\Delta|\omega_m} g\sqrt{n} = g_{ss}\sqrt{n} \tag{4.13}$$

Here, $g_{ss}$ is the single-phonon Rabi frequency for the sideband spin transition. For a time-domain experiment we set $\Delta = 100$ MHz. A relatively small detuning was employed such that effects of the excited state excitation can be investigated.

To determine the effective Rabi frequency of the sideband transition and effects of optical pumping, we measure the spin population in the $m_s = \pm 1$ states as a function of the duration of the optical driving fields. Figure 4.6(a) illustrates the pulse sequence used for the experiment. The circles in Fig. 4.6(b) show the fluorescence from state $A_2$ as a function of the optical pulse duration $\tau$ for the Raman resonant condition for states $|m_s = 0\rangle$ and $|m_s = +1, m_n = +1\rangle$, where $m_n$ denotes the nitrogen nuclear spin projection. The squares in Fig. 4.6(b) show fluorescence from $A_2$ when the optical fields are detuned 6.5 MHz away from the Raman resonant condition. This demonstrates the high rate of optical pumping from excitation and subsequent decay of the upper state into $m_s = +1$.

Using the density matrix equations, we plot theoretical predictions for these experiments in Fig. 4.6(b). We have taken $\Omega_R = \Omega_\pm$ and $\Gamma_1$, the decay rate from $E_y$ to the $m_s = \pm 1$ states as adjustable parameters. The calculations yield $\Gamma_1/2\pi = 1.8$ MHz and $\Omega_R/2\pi = 8$ MHz, which is in agreement with the Rabi frequency derived from the CPT experiments. These results yield an effective sideband Rabi frequency of $\Omega_{SS}/2\pi = 0.3$ MHz.

Both the optical pumping rate and the optically induced decoherence scale with the population of $E_y$ $(1/\Delta^2)$, because these processes only occur when the excited state is populated. Since we want to drive the sideband spin transition coherently we want to reduce spontaneous emission from $E_y$ to $m_s = \pm 1$. Their effects can be suppressed in the limit of large dipole detuning, however, $\Omega_{SS}$ scales as $1/\Delta$. By setting $\Omega_\pm/|\Delta|$ and $\Omega_0/|\Delta|$ to 1/60, we can keep $\gamma_{opt}/2\pi$ to 1 kHz. With $|\Delta| = 25\omega_m$,

Eq. 4.13 then produces a single-phonon Rabi frequency $g_{ss}$ that is three orders of magnitude greater than that of direct ground-state spin-phonon coupling.

In future experiments we would like to adiabatically transfer population between the $|m_s = 0\rangle$ and $|m_s = +1\rangle$ states but this interaction is limited by the dephasing time. The next chapter discusses preliminary efforts undertaken to protect the spin ground states from dephasing. The dephasing rate can be reduced by using the eigenstates of the atom-field Hamiltonian, which are protected from magnetic fluctuations.

# CHAPTER V

# MICROWAVE SPIN DRESSED STATES

## 5.1. Introduction

In a quantum system, an inhomogeneous environment can limit the coherence of a qubit. Solid-state spin qubits are highly susceptible to uncontrolled environmental noise such as magnetic fluctuations. The electron spin of a single NV center couples to magnetic fields from nearby nuclear spins in the diamond. The bath-induced fluctuations shorten the spin dephasing time $T_2^*$ of the system, which can limit complete quantum control. Pulsed dynamical decoupling (PDD) techniques[24, 57, 99, 145] use spin echoes to average out the effects of magnetic fluctuations and have been successfully implemented in NV centers and other spin qubits [20, 31, 32, 40, 96, 105, 127, 155]. Longer dynamical decoupling sequences weaken the signal and spin echo pulses do not always commute with gate operations[149]. Under these restrictions we use the semiclassical dressed states to protect the bare states from magnetic fluctuations.

Dressing the spin states of the NV center engineers a basis that is less sensitive to magnetic fluctuations. For NVs, a magnetic driving field interacts with the system such that the eigenstates of the interaction Hamiltonian are superpositions of the bare spin states. The dressed state energy level splitting is determined by the strength of the driving field and can be tuned to match the resonance of other quantum systems. An inhomogeneous background shifts the ground state energy levels, detuning the field from the transition. The effective separation between the dressed states is proportional to the dressing field and the detuning.

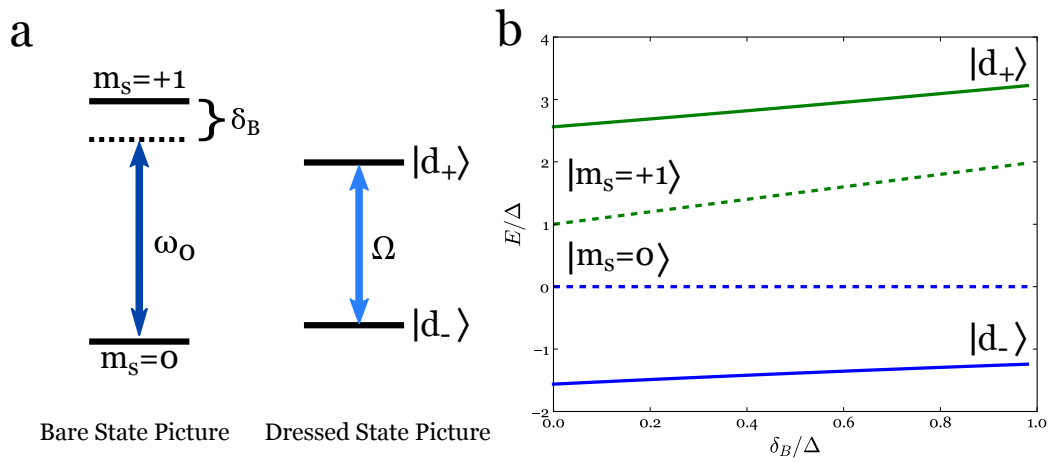


FIGURE 5.1. (a) The coupling of the $m_s = 0$ and $m_s = +1$ via a resonant microwave field with Rabi frequency $\Omega_0$ leads to the formation of the dressed states $|\pm\rangle$. The bath-induced Zeeman shift $\delta_B$ leads to an effective Rabi frequency $\Omega = \sqrt{\Omega_0^2 + \delta_B^2}$. (b) The eigenenergies as a function of $\delta_B$ for a weak dressing field (dashed line) $\Omega_0 = 0.1\Delta$. This resembles the bare states. For a strong dressing field (solid line) $\Omega_0 = 4\Delta$ the gap between the dress states remains unperturbed.

For a strong driving field this continuous dynamical decoupling (CDD) technique decouples the states from magnetic noise, prolonging the spin dephasing time. Additionally, CDD does not interfere with gate operations and protects gates from spin dephasing. Coherent dressing of the ground states in NV centers has been demonstrated using microwave (MW) fields and mechanical motion of a cantilever [13, 23, 49, 88, 91, 121, 136, 141, 143, 156, 161].

## 5.2. Dressed States

The Hamiltonian for the spin ground states of the NV center is

$$H_{gs} = D_{gs} S_z^2 + \gamma_B \vec{B} \cdot \vec{S}, \tag{5.1}$$

where $D_{gs}$ is the zero-field ground state splitting, $\gamma_B$ is the gyromagnetic ratio, $\vec{B}$ is a static magnetic field and $\vec{S}$ are the Pauli-spin matrices. A static magnetic field is

used to break the degeneracy between the $|\pm 1\rangle$ states. The dressed states of the NV center are formed by coupling a microwave field to the spin transition between the $m_s = 0$ and $m_s = +1$ states, with Rabi frequency $\Omega_0$. The electron wave function in the rotating frame is given by

$$|\psi\rangle = C_0|0\rangle + C_{+1}e^{-i\omega_L t}|+1\rangle \tag{5.2}$$

where $\omega_L$ is the microwave frequency. The Hamiltonian of the spin-microwave system is

$$H_0 = -\Delta|+1\rangle\langle+1| + \frac{\Omega_0}{2}(|0\rangle\langle+1| + |+1\rangle\langle 0|). \tag{5.3}$$

The detuning is $\Delta = -(\omega_L - \omega_0) + \delta_B$, with $\omega_0$ as the transition frequency and $\delta_B$ is the Zeeman shift induced by the bath. When the system is on resonance and $\delta_B = 0$, the eigenstates the time independent Hamiltonian are

$$|d_+\rangle = \frac{1}{\sqrt{2}}(|0\rangle + |+1\rangle) \tag{5.4}$$

$$|d_-\rangle = \frac{1}{\sqrt{2}}(|0\rangle - |+1\rangle), \tag{5.5}$$

with energy splitting $\Omega_0$. Here, the static magnetic field determines the resonance condition, while magnetic noise due to the spin-bath shifts the $|+1\rangle$ state by $\delta_B$ inducing a time-dependent detuning in the system. This perturbation changes the frequency splitting of the dressed states to $\Omega = \sqrt{\Omega_0^2 + \delta_B^2}$, as illustrated in Fig. 5.1(a), and the new dressed states are

$$|d_+\rangle = \sin\theta|0\rangle + \cos\theta|+1\rangle \tag{5.6}$$

$$|d_-\rangle = \cos\theta|0\rangle + \sin\theta|+1\rangle \tag{5.7}$$

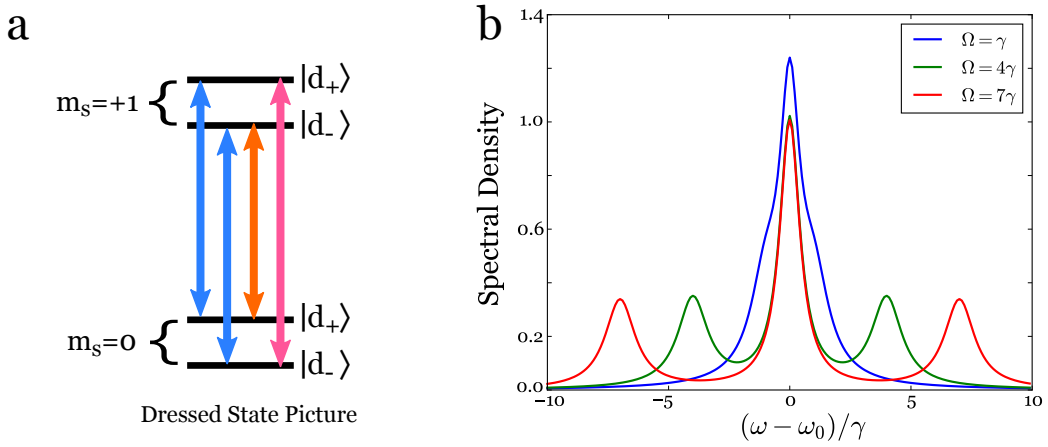


FIGURE 5.2. (a) Energy level diagram of the dressed state manifolds depending on photon number. The orange transition denotes the central peak at frequency $\omega = \omega_0$, the orange and pink transitions occur at $\omega = \omega_0 - \Omega$ and $\omega = \omega_0 + \Omega$, respectively. (b) Simulated Mollow triplet for three different effective Rabi frequencies.

where $\tan 2\theta = \Omega_0/\delta_B$. The corresponding eigenenergies of the dressed states are $E_+ = \hbar\Omega/2$ and $E_- = -\hbar\Omega/2$. In the limit $\Omega_0 \gg |\delta_B|$, the dressed states are insensitive to inhomogeneities in the system. Figure 5.1(b) shows the dependence of the two-level system eigenenergies on the magnetic fluctuations $\delta_B$. For a weak dressing field $\Omega_0 = 0.1\Delta$, the eigenstates resemble the bare states $\{|m_s = 0\rangle, |m_s = +1\rangle\}$. In the limit $\Omega_0 = 4\Delta \gg \delta_B$, the dressed states become independent of $\delta_B$.

### 5.3. Mollow Triplet

The dressed states have been observed by driving coherent Rabi oscillations in single spins [63, 75, 118] and coherent population trapping using the excited state optical transitions [49]. In this work, we measure the Mollow spectrum to observe the dressed states of the system [6, 79, 102, 160].

We now consider the interaction of the electron spin with a strong microwave to form the dressed spin states and a weak probe for driving interactions between the dressed states. We use the dressed states to describe the electron wave function in

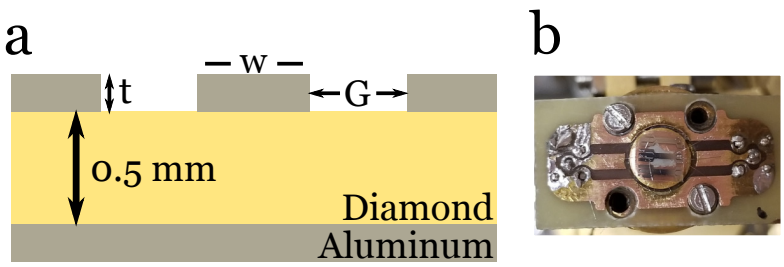


FIGURE 5.3. (a) Schematic of coplanar waveguide. (b) Image of RF device used for applying microwaves to the NV center.

terms of the dressed-state probability amplitudes, $C_{d_+}$ and $C_{d_-}$:

$$\begin{aligned} |\psi\rangle = &\left(C_{d_+}\sin\theta e^{-i\Omega t/2} + C_{d_-}\cos\theta e^{i\Omega t/2}\right)|0\rangle \\ &+ \left(C_{d_+}\cos\theta e^{-i\Omega t/2} + C_{d_-}\sin\theta e^{i\Omega t/2}\right)|+1\rangle \end{aligned} \tag{5.8}$$

A similar expression can be derived for $\delta_B = 0$, in which $\cos\theta = \sin\theta = 1/\sqrt{2}$. The wave function in Eq. 5.8 shows that the $m_s = 0, +1$ states each effectively split into two states due to the coherent interaction with the microwave field, as shown in Fig. 5.2(a). Spin coherence can arise from the same dressed, for example between $|d_+\rangle_{+1}$ and $|d_+\rangle_0$, and can also occur between different dressed states, like $|d_+\rangle_{+1}$ and $|d_-\rangle_0$. The resulting power correlation spectrum from scanning the probe frequency is the Mollow triplet. Figure 5.2(b) displays the Mollow triplet for three different driving powers as a function of the probe detuning. The central peak is at frequency $\omega_0$ with symmetrical side peaks at $\omega_0 \pm \Omega$. Two transitions have the same frequency $\omega_0$, depicted in Fig. 5.2(a) in blue, making the central peak dominant.

### 5.4. Experimental Results

We use a coplanar waveguide (CPW) to generate the microwave fields on a type-IIa diamond with ppb nitrogen impurities. We find a NV center a few microns

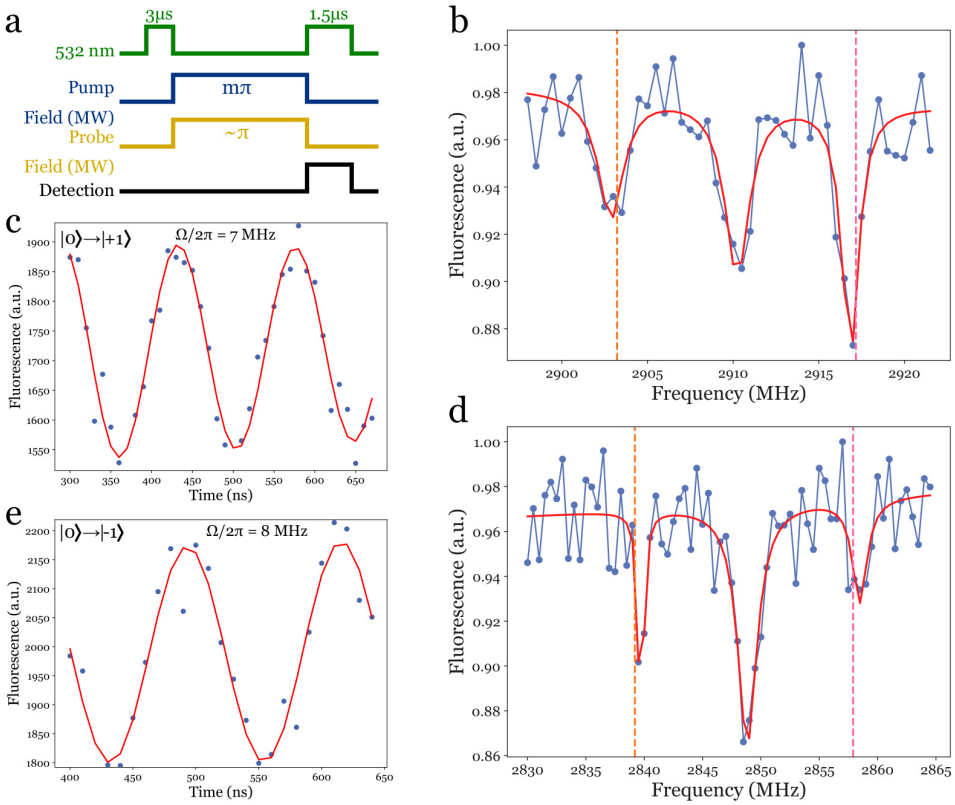


FIGURE 5.4. (a) Pulse sequence for Mollow spectrum experiment. (b) Mollow spectrum of the dressed electron spin for bare states $|0\rangle$ and $|+1\rangle$. The pump and probe powers are $P_{pump} = 6$ dBm and $P_{probe} = -9$ dBm, respectively. (c) Rabi oscillation experiment for the pump power in (b) and derived Rabi frequency $\Omega_0 = 6.97$ MHz. (d) Mollow triplet for the two-level system of states $|0\rangle$ and $|-1\rangle$. (e) Rabi oscillation experiment for $P_{pump} = 7$ dBm with derived Rabi frequency $\Omega_0 = 8.1$ MHz.

beneath the surface to suppress background noise and thus choose to use a grounded CPW which ensures the magnetic field is strongest in the diamond. Figure 5.3(a) illustrates the CPW transmissions lines with $G = 15\mu m$ and $w = 100\mu m$ for our device. We deposited a 200 nm layer of Al on top of a 10 nm Ti adhesion layer to impedance match our device to 50 Ohms. The microwave device is bonded to a PCB chip with two ports, an input port for the signal and an output port where the signal is terminated to reduce back reflections into the CPW (see Fig. 5.3(b)).

First we initialize the electron spin into the $m_s = 0$ ground state and then simultaneously apply a strong pump field and a weak probe. The high-power MW field, with duration $\tau$ creates the dressed states with splitting equal to the Rabi frequency $\Omega_0$. We can keep track of the location of the population by choosing $\tau$ to be a multiple of $\pi$. The decoherence time in our system is $\approx 1.2\mu s$, limiting our pulse lengths to $< 1\mu s$ for better readout. A weak $\pi$-pulse probe field drives four different transitions as depicted in Fig. 5.2(a). We do optical readout on the $m_s = 0$ state as shown in the pulse sequence in Fig. 5.4(a). We obtain the Mollow triplet when we scan the probe frequency.

In Fig. 5.4(b), we plot the population of the ground state as a function of the probe frequency, which is swept close to the resonance. The pump power was held constant at $P_{pump}$ = 7 dBm (at the source) while the probe was kept at $P_{probe}$ = -9 dBm (at the source). The spectrum consists of a central peak with two side peaks with separation $2\Omega$, following the Mollow structure. The red lines in Fig. 5.4(b) are Lorentzian fits to each dip which we used to derive a Rabi frequency of $\Omega/2\pi \approx 7$ MHz. We performed a Rabi oscillation experiment at the same MW pump power shown in Fig. 5.4(c) and fit it to $f(x) = A_0 \cos(2\pi\Omega t + \phi)e^{-\gamma t}$. The Rabi frequency for this experiment is $\Omega/2\pi \approx 7$ MHz and is used to plot the expected sideband frequency in orange and pink in Fig. 5.4(b). Our calculated values were in excellent agreement with the experimental values. We carried out the same similar experiment with the $m_s = 0$ and $m_s = -1$ states as shown in Fig. 5.4(d) with RF powers $P_{pump}$ = 7 dBm and $P_{probe}$ = -13 dBm at the source. From our Lorentzian fit to the data we extracted a Rabi frequency $\Omega/2\pi \approx 9$ MHz. The Rabi oscillation experiment shown in Fig. 5.4(e) yielded a Rabi frequency of $\Omega/2\pi \approx 8$ MHz for the same pump power.

Our spectra display dips instead of peaks because of the number of $\pi$ rotations. For these experiments we apply a pump fields with length $\tau = 8\pi$ and the electron spin populates the lower manifold. The probe field then pumps the population into the upper manifold of the system on resonance. The spin-readout detects fluorescence from the $m_s = 0$ state and on resonance the upper manifold fluoresces less causing a dip in fluorescence. If we extend our pump pulse length to $\tau = 9\pi$, we could recover the peaks because the probe field would move the population of the electron spin into the $m_s = 0$ components of the dressed states and during readout the fluorescence would be higher.

Figures 5.4(b) and (d) do not reflect the true structure of the Mollow triplet and manifest asymmetries due to systematic errors in the system. Long averaging times were used to obtain a better signal-to-noise ratio, however, these long experimental times are susceptible to drift. Future experiments will combine the dressed states with optical control for direct spin readout, improving the experimental time and signal-to-noise ratio.

For quantum information science, using the dressed states of the NV center as the qubit has an advantage over the bare states. The dressed states are protected against magnetic fluctuations of the bath, allowing for longer quantum control protocols that do not conflict with the dressing field. We used a pump-probe experiment to detect the existence of the dressed states by observing the Mollow triplets spectrum. At room temperature, we demonstrate control and spin readout of our system.

Another interesting property of our system is that we can couple the dressed states to a shared excited state using optical fields for coherent population transfer, as shown previously[49]. This allows us to use the dressed states in the spin-phonon $\Lambda$-type three level system, as shown in Fig. 5.5. In the next chapter, we discuss

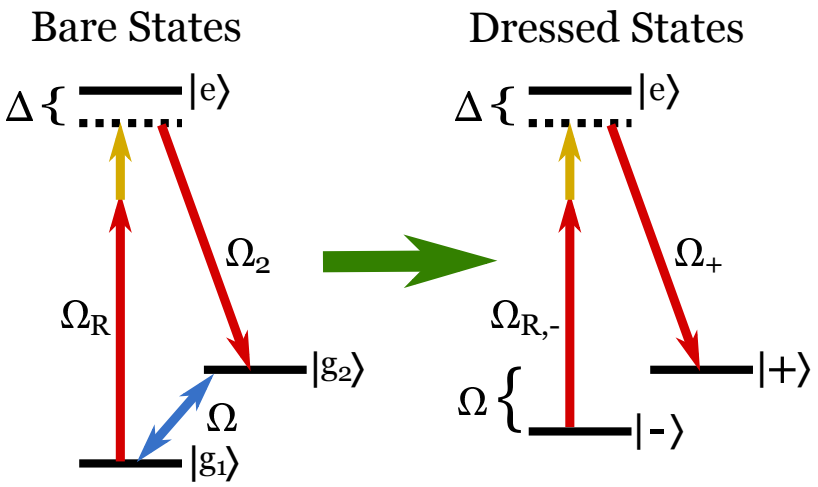


FIGURE 5.5. Spin-phonon Λ-type three level system in the bare state and dressed state basis. $\Omega_R$ denotes the red sideband Rabi frequency for the $|g_1\rangle$ state and $\Omega_{R,-}$ is the red sideband Rabi frequency for the $|-\rangle$ dressed state. The MW field applied to the ground states has a Rabi frequency $\Omega$, which defines the splitting between the dressed states.

a technique to improve adiabatic transfer via the dark state in a Λ-system. This method will improve the fidelity and limit the decoherence due to the excited state without needing a large detuning. The goal is to have a robust spin-phonon system with a strong phonon-sideband interaction.

# CHAPTER VI

# SHORTCUT-TO-ADIABATICITY IN A Λ-TYPE THREE-LEVEL SYSTEM

## 6.1. Introduction

A variety of methods exist for transferring population between two quantum states, most notably adiabatic processes are known for being robust and yielding high fidelities [152]. Stimulated Raman adiabatic passage has been demonstrated in NV centers in which two driving fields, which couple the lower states to a common upper state, are pulsed to adiabatically follow the dark state [52]. However, the system contains non-adiabatic processes that populate the upper state making it susceptible to loss. It was first proposed in 1997 that a field could be applied between the two quantum states that would "control diabatic losses" [146]. Recently, superadiabatic transitionless driving (SATD) was proposed and experimentally demonstrated as an alternative because usually transitions are not allowed between the states that exchange population [8, 162]. In this chapter we demonstrate that a shortcut-to-adiabaticity technique (STA) can be employed for our special Λ-type three level system.

## 6.2. Theory of Shortcut-to-Adiabatic Passage

Stimulated Raman adiabatic passage (STIRAP) is a quantum state transfer process in which population from an initial state $|g_1\rangle$ is transferred to a target state $|g_2\rangle$, through two optical fields via an intermediate state $|e\rangle$. Here, we consider a Λ-type three-level system with pump and Stokes fields coupling $|g_1\rangle$ to $|e\rangle$ and $|g_2\rangle$ to $|e\rangle$, respectively, as illustrated in Fig. 6.1(a). The system adiabatically follows

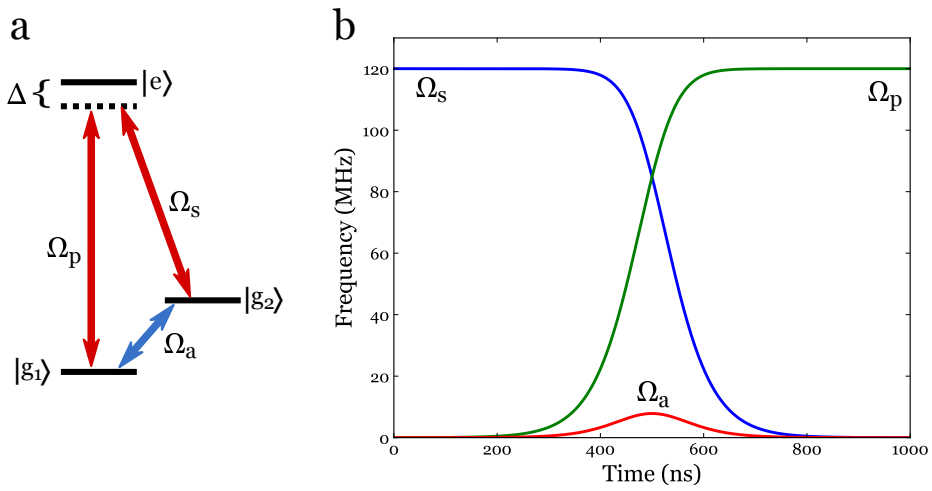


FIGURE 6.1. (a) Λ-type three-level system with pump field $\Omega_p$ and Stokes field $\Omega_s$. In this case $\Omega_a = 2\dot{\theta}(t)$ denotes the counterdiabatic field that cancels the non-adiabatic effects. (b) Pulse shape for the three fields applied to the Λ-system in (a).

a quantum state independent of $|e\rangle$, also known as the dark state, thus making the transfer process immune to spontaneous emission.

The interaction Hamiltonian for a Λ-type three-level system with the rotating wave approximation is given by:

$$H_I(t) = \begin{pmatrix} 0 & \Omega_p(t) & 0 \\ \Omega_p(t) & 2\Delta & \Omega_s(t) \\ 0 & \Omega_s(t) & 0 \end{pmatrix} \tag{6.1}$$

where $\Omega_p$ and $\Omega_s$ are the Rabi frequencies for the pump and Stokes fields, respectively, and $\Delta = (\omega_e - \omega_1) - \omega_p = (\omega_e - \omega_2) - \omega_s$ is the constant detuning. The Hamiltonian in Eq. 6.1 has three instantaneous eigenstates

$$\begin{aligned} |u(t)\rangle &= \sin\theta \sin\phi |g_1\rangle + \cos\theta \sin\phi |g_2\rangle + \cos\phi |e\rangle \\ |d(t)\rangle &= \cos\theta |g_1\rangle - \sin\theta |g_2\rangle \\ |l(t)\rangle &= \sin\theta \cos\phi |g_1\rangle + \cos\theta \cos\phi |g_2\rangle - \sin\phi |e\rangle \end{aligned} \tag{6.2}$$

with eigenvalues $E_u = \hbar\Omega \cot \phi/2$, $E_d = 0$, and $E_l = -\hbar\Omega \tan \phi/2$. The mixing angles are defined by $\tan\theta = \Omega_p(t)/\Omega_s(t)$, and $\tan 2\phi = \frac{\Omega}{\Delta}$, where $\Omega = \sqrt{\Omega_p^2(t) + \Omega_s^2(t)}$.

The pump and Stokes fields are pulsed such that at an initial time $t_i$ the dark state is $|d(t_i)\rangle = |g_1\rangle$ and slowly evolves to a final state $|d(t_f)\rangle = |g_2\rangle$. The pump and Stokes pulses have a Vitanov shape (see Fig. 6.1(b)), the optimal pulse shape for STIRAP [151], defined by the equations below:

$$\begin{aligned} \Omega_p(t) &= \Omega_{0,p} \sin\theta(t) \\ \Omega_s(t) &= \Omega_{0,s} \cos\theta(t) \\ \theta(t) &= \frac{\pi}{2} \frac{1}{1 + e^{-v(t-L/2)}}, \end{aligned} \tag{6.3}$$

where $\Omega_0$ is the amplitude of the field, L is a delay, and $v$ determines the rate of the adiabatic sweep. Figure 6.2(a) displays the time evolution of the three bare states for the STIRAP protocol. While the transfer seems complete and the population of the excited state is suppressed the dressed state basis paints a different picture. The solid lines in Fig. 6.2(b) show the dynamics of the dressed state basis, in which the initial state is $|d\rangle$ but during the interaction the dressed state $|l\rangle$ is also populated. Since $|l\rangle$ has an excited state component it would induce loss in the system.

Studying the Hamiltonian in the dressed state basis, where the eigenstates are time-independent, demonstrates the dynamics that populate $|e\rangle$. The dressed Hamiltonian gets transformed as

$$H_D = U H_I U^\dagger - i\hbar U \frac{\partial U^\dagger}{\partial t}, \tag{6.4}$$

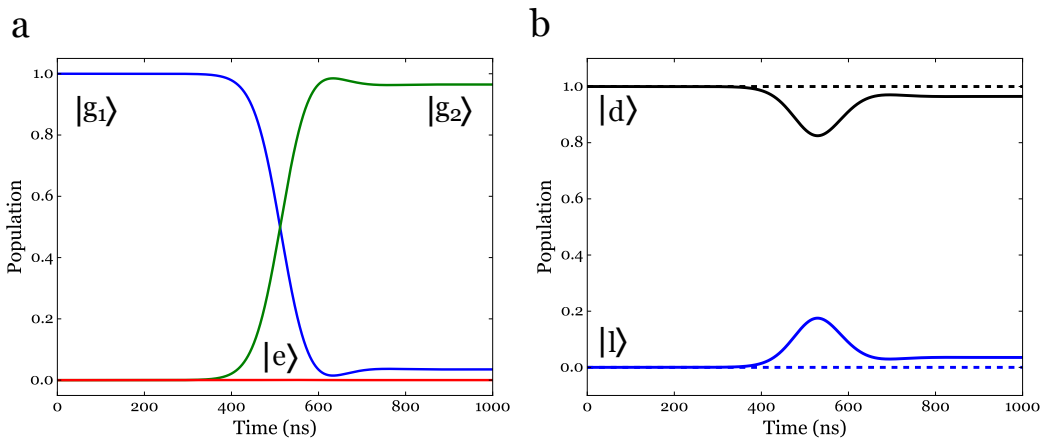


FIGURE 6.2. (a) Population of the three states as a function of time during the STIRAP protocol. The optical Rabi frequencies are $\Omega_{0,p} = \Omega_{0,s} = 2\pi \times 120$ MHz and detuning $\Delta = 2\pi \times -1.0$ MHz. (b) In the dressed state basis, at time $t_i = 0$ the dark state is initially populated but the state $|l\rangle$ becomes populated due to a coupling between the dressed states. The solid lines shows the dynamics for a STIRAP experiment and the dashed lines includes a counterdiabatic term that negates the coupling between $|d\rangle$ and $|l\rangle$.

where U is the unitary transformation that maps the bare states onto the dressed state basis,

$$U(t) = \begin{pmatrix} \sin\theta\sin\phi & \cos\phi & \cos\theta\sin\phi \\ \cos\theta & 0 & -\sin\theta \\ \sin\theta\cos\phi & -\sin\phi & \cos\theta\cos\phi \end{pmatrix} \tag{6.5}$$

The second term of Eq. 6.4 leads to non-adiabatic excitations,

$$U(t)\frac{\partial U^{\dagger}(t)}{\partial t} = \begin{pmatrix} 0 & -\dot{\theta}\sin\phi & -\dot{\phi} \\ \dot{\theta}\sin\phi & 0 & \dot{\theta}\cos\phi \\ -\dot{\phi} & -\dot{\theta}\cos\phi & 0 \end{pmatrix} \tag{6.6}$$

where $\dot{\theta} = (\dot{\Omega}_p\Omega_s - \dot{\Omega}_s\Omega_p)/\Omega^2$ and $\dot{\phi} = [\Delta(\dot{\Omega}_p\Omega_p + \dot{\Omega}_s\Omega_s)]/[2\Omega(\Delta^2 + \Omega^2)]$. The $\dot{\phi}$ term couples the dressed states $|u\rangle, |l\rangle$ and does not affect the adiabatic transfer in question. In comparison, $\dot{\theta}$ couples the dark state $|d\rangle$ to the other dressed states

allowing transitions to the intermediate state $|e\rangle$. In order to prevent transitions to $|e\rangle$, a correction term $H_{CD}$ can be added to the Hamiltonian such that it cancels out the non-adiabatic driving [18, 26, 33, 146]:

$$\begin{aligned} H_D &= U(H_I + H_{CD})U^\dagger - i\hbar U\frac{\partial U^\dagger}{\partial t} \\ H_D &= UH_IU^\dagger + \underbrace{UH_{CD}U^\dagger - i\hbar U\frac{\partial U^\dagger}{\partial t}}_{=0} \end{aligned} \tag{6.7}$$

This transitionless driving, or counter-diabatic term is a direct transition between the $|g_1\rangle$ and $|g_2\rangle$ states in the bare state basis. Here we ignore any terms that depend on $\dot{\phi}$ since it would require additional fields and those terms do not contribute to the adiabatic transfer.

$$H_{CD}(t) = i\hbar\frac{\partial U^\dagger}{\partial t}U = i\hbar\begin{pmatrix} 0 & 0 & \dot{\theta} \\ 0 & 0 & 0 \\ -\dot{\theta} & 0 & 0 \end{pmatrix} \tag{6.8}$$

By adding $H_{CD}$ to the Hamiltonian, only the dark state is populated, as shown by the dashed lines in Fig. 6.2(b), and the excited state population is completely suppressed.

## 6.3. Suppressing the Excited State Population

### 6.3.1. Λ-type Three-level Systems

In Λ-type three-level systems, usually transitions between $|g_1\rangle$ and $|g_2\rangle$ are dipole forbidden and STIRAP is used as an alternative method to transfer population between these states. The NV center is no different in that a three-level system cannot

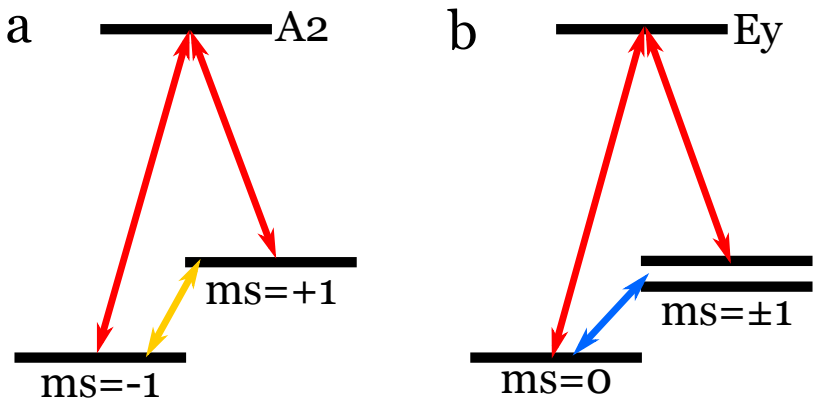


FIGURE 6.3. Two different Λ-type three-level systems, where the red arrows represent optical fields, the yellow arrow a mechanical field, and the blue arrow a microwave field. (a) The $m_s = \pm$ states share an excited state $A_2$ and can couple to each other via mechanical strain. (b) High strain induces spin-mixing in the excited state energy levels allowing $m_s = 0$ and $m_s = \pm 1$ to both couple to $E_y$.

have a third optical field. For example, the $m_s = 0$ state can couple to the $m_s = \pm 1$ states through microwave fields but they do not share an excited state because their direct optical dipole transitions are spin-preserving. The next choice would be to use the $m_s = \pm 1$ states because they can share a common excited state but transitions between these two states are forbidden. However, by exploiting the strain properties of the NV center two different closed-loop Λ-systems can be accessed as shown in Fig. 6.3. As discussed in Chapter 3, transverse strain in the ground state allows the $m_s = \pm 1$ states to be coupled through mechanical motion. This mechanical coupling has been experimentally demonstrated using a diamond cantilever with NV centers [13], making it a feasible system. The second Λ-type energy structure is accessible at large strain. In Chapter 4, we studied the effects of strain on the excited state energy levels and noticed that a high strain environment causes mixing of the lower orbital branch. The symmetry properties are broken, allowing optical non-spin preserving transitions to occur. Here, we choose the Λ-system in Fig. 6.3(b), where $m_s$ shares a

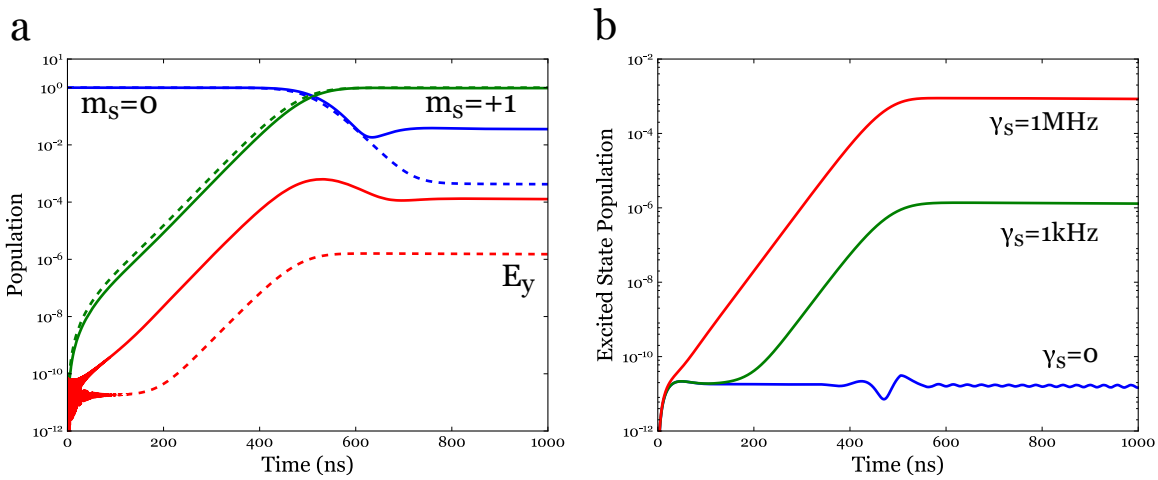


FIGURE 6.4. Adiabatic passage (a) Theoretical calculations for STIRAP with (dashed line) and without (solid line) STA using the pulse parameters in Fig. 6.1(b) and decay terms from Eq. 6.10. (b) Excited state population for different dephasing rates with the STA protocol.

common state with $m_s = \pm 1$, as a model system for transitionless quantum driving to minimize the population of the excited state $E_y$.

### 6.3.2. Numerical Analysis of STA

We numerically solve the optical Bloch equations given by

$$\dot{\rho} = -i[H_I + H_{CD}, \rho] - D(\rho) \tag{6.9}$$

with

$$D(\rho) = \begin{pmatrix} \Gamma\rho_{ee} & -\gamma\rho_{0e} & -\gamma_s\rho_{0+} \\ -\gamma\rho_{e0} & -2\Gamma\rho_{ee} & -\gamma\rho_{e+} \\ -\gamma_s\rho_{+0} & -\gamma\rho_{+e} & \Gamma\rho_{ee} \end{pmatrix}, \tag{6.10}$$

where $\Gamma = \gamma = 2\pi \times 14$ MHz and $\gamma_s = 2\pi \times 1.0$ kHz.

In preliminary numerical simulations, we demonstrate that the excited state population can be reduced by a factor of $10^2$ for an isotropically pure diamond,

where we assume a dephasing rate $\gamma_s = 1$ kHz. Figure 6.4(a) plots the population of $\{|0\rangle, |+1\rangle, |E_y\rangle\}$ as a function of time for two different adiabatic passage protocols. The dashed lines display STIRAP with counterdiabatic driving. The optical Rabi frequencies of the pump and probe field are $\Omega_{0,p} = \Omega_{0,s} = 2\pi \times 120$ MHz and detuning $\Delta = 2\pi \times 1.0$ GHz. These parameters were chosen based on results from previous experiments. Additionally, the delay $L$ and adiabatic sweep $v$ parameters that define the pulse shapes play a crucial role in deciding the Rabi frequency of the counterdiabatic field. We set $v = 0.02$ and $L = 1000$ to produce a counterdiabatic field with maximum Rabi frequency $\dot{\theta}/2\pi = 8$ MHz, which we were able to achieve with our microwave coplanar waveguide in Chapter 5. Shorter timescales would require higher microwave Rabi frequencies. The dephasing rate plays a crucial role in STIRAP because dephasing destroys the coherence between the spin states, thus populating other eigenstates of the interaction Hamiltonian. In the adiabatic limit the population of the three states depends on the dephasing between $m_s = 0$ and $m_s = +1$ [61]. The effect of STA on the excited state is diminished with higher dephasing rates as shown in Fig. 6.4(b). Longer dephasing times depend on the purity of the diamond and the concentration of NV centers.

One of the benefits of using the shortcut-to-adiabaticity method is that it can be used at shorter interaction times while satisfying the adiabatic condition. At shorter timescales dephasing losses decrease and the Rabi frequencies of the pump and Stokes do not influence the adiabatic solution [61]. In Fig. 6.5(a), we compare the excited state population as a function of time for a dephasing rate $\gamma_s = 2\pi \times 1.0$ MHz at longer (blue) and shorter (green) interaction times with and without STA (dashed lines). The blue (green) lines in Fig. 6.5(a) have an adiabatic sweep parameter of $v = 0.02$ ($v = 0.08$). The higher dephasing rate increases the excited state population

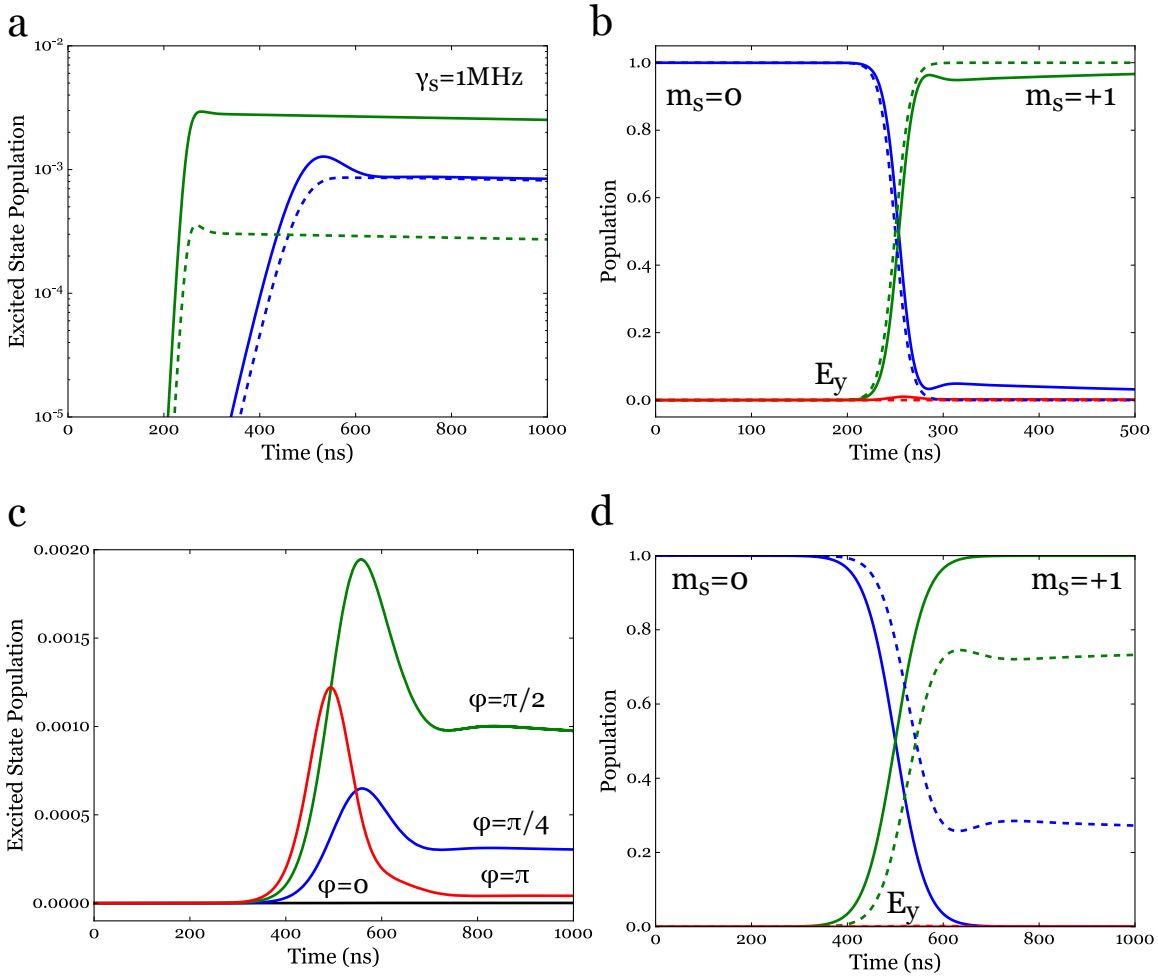


FIGURE 6.5. (a) Excited state population versus time for different interaction times. The blue lines depict dynamics with $v = 0.02$ and the green lines at $v = 0.08$. The dashed lines denote the use of a counterdiabatic term. (b) Adiabatic passage for a shorter interaction time with the use of STA (dashed line). (c) Excited state population as a function of time for $\Omega_a = 2\dot{\theta}(t)e^{i\phi}$. (d)Dynamics of the system for STA with $\phi = 0$ (solid lines) and $\phi = \pi/2$ (dashed line).

but our simulations demonstrate that there is still an advantage in using STA while providing faster population inversion. Figure 6.5(b) shows the populations of the three states as a function of time for a shorter interaction time. The dashed lines have the counterdiabatic field, suppressing the excited state population and allowing a full transfer.

One of the disadvantages of STA is that a closed loop system is sensitive to the phase of the fields. We added a phase factor to the counterdiabatic driving field and plotted the excited state population versus time in Fig. 6.5(c). The excited state is least affected by the transitionless driving when $\phi = \pi/2$, the green line. It interferes with the optical fields in such a way that the population inversion cannot complete (see Fig. 6.5(d)). Figure 6.5(d) demonstrates the population of the three states as a function of time for the STA technique for $\phi = 0$ (solid lines) and $\phi = \pi/2$ (dashed lines). The counterdiabatic field must be in phase to minimize the excited state population and complete the population transfer between the lower states. One explanation for this behavior is that the dark state is not decoupled from the system unless $\phi = 0$ [22].

The goal is to use the STA technique on the phonon-assisted $\Lambda$-scheme to increase the Rabi frequency of the sideband spin transition and combat the effects of optical pumping discussed in Chapter 4. This method can also be combined with the dressed states to protect the spin qubit from magnetic fluctuations of the nuclear spin bath. However, the system becomes more complicated because five fields are required to manipulated this $\Lambda$-type system.

# CHAPTER VII

# CONCLUSION

The experimental results reported in this dissertation aims to further investigate the interactions between solid-state systems and phonons. This work lays down the groundwork to build phononic devices to interface multiple quantum systems and mediate interactions between solid-state spins. The techniques studied to reduce decoherence will help preserve the quantum state of the system for storing and transferring of quantum information.

In this dissertation, we coupled a surface acoustic wave to the electron spin of a nitrogen vacancy (NV) center in diamond. We demonstrated optomechanical control through the strong excited state electron-phonon coupling. Using the phonon sidebands, we realized Rabi oscillations between the ground state $m_s = 0$ and excited state $E_y$. In addition, we observed quantum interferences between a phonon-assisted optical transition and the direct dipole optical transition. We studied the strain dependent frequency splitting in the excited states to select a $\Lambda$-type three-level system which allows non-spin preserving transitions. Through this $\Lambda$-system we realize strong spin-mechanical coupling via a dark state. We perform coherent population trapping experiments to demonstrate the formation of a dark state with an acoustic wave. Finally, we demonstrate coherent driving of these spin sideband transitions and study the effects of optical pumping on our system. This work confirms the fundamental mechanisms that will be used for coupling distant NV spins via mechanical vibrations.

We discuss two methods to protect the spin state from decoherence. The first method uses a strong microwave field to create the dressed states, which are less

sensitive to a fluctuating magnetic environment. We built a microwave device to effectively apply strong microwave fields to the NV center and acquire a Mollow triplet fluorescence spectrum demonstrating the formation of dressed states in our system. The second method is the shortcut-to-adiabaticity, in which a field between the lower states of a Λ-system is used to reduce the population of the excited state. This counterdiabatic field forces the system to follow the dark state and reduces spontaneous emission due to coupling to the excited state.

### 7.1. Future Directions

We have only scratched the surface of this area and have yet to control the spin and mechanical degrees of freedom in the NV center. The next generation of surface acoustic wave (SAW) experiments will feature adiabatic passage through phonon-assisted transitions and driving spin transitions in the excited state with phonons. Additionally, we can build SAW devices with lower frequencies to drive spin $\Delta m_s = \pm 2$ transitions that are magnetically forbidden. Our work will also investigate coupling acoustic waves to a spin ensemble for use in quantum memories.

The dressed state formalism can be used in combination with the Λ-systems that feature a phonon interaction to extend the spin coherence. Since $|m_s = -1\rangle \rightarrow |m_s = +1\rangle$ cannot be driven magnetically we can circumvent this by using the dressed states. We propose experiments demonstrating population transfer between the dressed states $\{|+\rangle, |-\rangle\}$ and the third bare ground state $|-1\rangle$. Then we can use this technique to do stimulated Raman adiabatic passage via a phonon-sideband optical transition to further decouple the system from a radiative excited state.

This work can be extended to other defects in diamond such as silicon vacancy centers [126, 134] and germanium vacancy centers [62, 135]. These color centers

feature stronger ZPLs compared to that of the NV. Since entanglement between spins depends on photons emitted from the ZPL [17], silicon and germanium vacancies could be used to realize higher entanglement rates between distant centers via mechanical motion.

REFERENCES CITED


[1] Acosta, V., Bauch, E., Ledbetter, M., Waxman, A., Bouchard, L.-S., and Budker, D. (2010). Temperature dependence of the nitrogen-vacancy magnetic resonance in diamond. *Physical review letters*, 104(7):070801.

[2] Acosta, V. M., Bauch, E., Ledbetter, M. P., Santori, C., Fu, K.-M. C., Barclay, P. E., Beausoleil, R. G., Linget, H., Roch, J. F., Treussart, F., Chemerisov, S., Gawlik, W., and Budker, D. (2009). Diamonds with a high density of nitrogen-vacancy centers for magnetometry applications. *Phys. Rev. B*, 80:115202.

[3] Albrecht, A., Retzker, A., Jelezko, F., and Plenio, M. B. (2013). Coupling of nitrogen vacancy centres in nanodiamonds by means of phonons. *New Journal of Physics*, 15(8):083014.

[4] Arcizet, O., Jacques, V., Siria, A., Poncharal, P., Vincent, P., and Seidelin, S. (2011). A single nitrogen-vacancy defect coupled to a nanomechanical oscillator. *Nature Physics*, 7(11):879.

[5] Aspelmeyer, M., Kippenberg, T. J., and Marquardt, F. (2014). Cavity optomechanics. *Rev. Mod. Phys.*, 86:1391–1452.

[6] Astafiev, O., Zagoskin, A. M., Abdumalikov, A., Pashkin, Y. A., Yamamoto, T., Inomata, K., Nakamura, Y., and Tsai, J. (2010). Resonance fluorescence of a single artificial atom. *Science*, 327(5967):840–843.

[7] Babinec, T. M., Choy, J. T., Smith, K. J., Khan, M., and Lončar, M. (2011). Design and focused ion beam fabrication of single crystal diamond nanobeam cavities. *Journal of Vacuum Science & Technology B, Nanotechnology and Microelectronics: Materials, Processing, Measurement, and Phenomena*, 29(1):010601.

[8] Baksic, A., Ribeiro, H., and Clerk, A. A. (2016). Speeding up adiabatic quantum state transfer by using dressed states. *Physical review letters*, 116(23):230503.

[9] Balasubramanian, G., Lazariev, A., Arumugam, S. R., and Duan, D.-w. (2014). Nitrogen-vacancy color center in diamond?emerging nanoscale applications in bioimaging and biosensing. *Current opinion in chemical biology*, 20:69–77.

[10] Balasubramanian, G., Neumann, P., Twitchen, D., Markham, M., Kolesov, R., Mizuochi, N., Isoya, J., Achard, J., Beck, J., Tissler, J., et al. (2009). Ultralong spin coherence time in isotopically engineered diamond. *Nature materials*, 8(5):383.

[11] Bar-Gill, N., Pham, L. M., Belthangady, C., Le Sage, D., Cappellaro, P., Maze, J., Lukin, M. D., Yacoby, A., and Walsworth, R. (2012). Suppression of spin-bath dynamics for improved coherence of multi-spin-qubit systems. *Nature communications*, 3:858.

[12] Bar-Gill, N., Pham, L. M., Jarmola, A., Budker, D., and Walsworth, R. L. (2013). Solid-state electronic spin coherence time approaching one second. *Nature communications*, 4:1743.

[13] Barfuss, A., Teissier, J., Neu, E., Nunnenkamp, A., and Maletinsky, P. (2015). Strong mechanical driving of a single electron spin. *Nature Physics*, 11(10):820.

[14] Batalov, A., Jacques, V., Kaiser, F., Siyushev, P., Neumann, P., Rogers, L., McMurtrie, R., Manson, N., Jelezko, F., and Wrachtrup, J. (2009a). Low temperature studies of the excited-state structure of negatively charged nitrogen-vacancy color centers in diamond. *Physical review letters*, 102(19):195506.

[15] Batalov, A., Jacques, V., Kaiser, F., Siyushev, P., Neumann, P., Rogers, L. J., McMurtrie, R. L., Manson, N. B., Jelezko, F., and Wrachtrup, J. (2009b). Low temperature studies of the excited-state structure of negatively charged nitrogen-vacancy color centers in diamond. *Phys. Rev. Lett.*, 102:195506.

[16] Bennett, S., Yao, N. Y., Otterbach, J., Zoller, P., Rabl, P., and Lukin, M. D. (2013). Phonon-induced spin-spin interactions in diamond nanostructures: application to spin squeezing. *Physical review letters*, 110(15):156402.

[17] Bernien, H., Hensen, B., Pfaff, W., Koolstra, G., Blok, M., Robledo, L., Taminiau, T., Markham, M., Twitchen, D., Childress, L., et al. (2013). Heralded entanglement between solid-state qubits separated by three metres. *Nature*, 497(7447):86.

[18] Berry, M. (2009). Transitionless quantum driving. *Journal of Physics A: Mathematical and Theoretical*, 42(36):365303.

[19] Blais, A., Huang, R.-S., Wallraff, A., Girvin, S. M., and Schoelkopf, R. J. (2004). Cavity quantum electrodynamics for superconducting electrical circuits: An architecture for quantum computation. *Physical Review A*, 69(6):062320.

[20] Bluhm, H., Foletti, S., Neder, I., Rudner, M., Mahalu, D., Umansky, V., and Yacoby, A. (2011). Dephasing time of gaas electron-spin qubits coupled to a nuclear bath exceeding 200 $\mu$s. *Nature Physics*, 7(2):109.

[21] Bochmann, J., Vainsencher, A., Awschalom, D. D., and Cleland, A. N. (2013). Nanomechanical coupling between microwave and optical photons. *Nature Physics*, 9(11):712.

[22] Buckle, S., Barnett, S., Knight, P., Lauder, M., and Pegg, D. (1986). Atomic interferometers. *Optica Acta: International Journal of Optics*, 33(9):1129–1140.

[23] Cai, J., Naydenov, B., Pfeiffer, R., McGuinness, L. P., Jahnke, K. D., Jelezko, F., Plenio, M. B., and Retzker, A. (2012). Robust dynamical decoupling with concatenated continuous driving. *New Journal of Physics*, 14(11):113023.

[24] Carr, H. Y. and Purcell, E. M. (1954). Effects of diffusion on free precession in nuclear magnetic resonance experiments. *Physical review*, 94(3):630.

[25] Chan, J., Alegre, T. M., Safavi-Naeini, A. H., Hill, J. T., Krause, A., Gröblacher, S., Aspelmeyer, M., and Painter, O. (2011). Laser cooling of a nanomechanical oscillator into its quantum ground state. *Nature*, 478(7367):89.

[26] Chen, X., Lizuain, I., Ruschhaupt, A., Guéry-Odelin, D., and Muga, J. G. (2010). Shortcut to adiabatic passage in two- and three-level atoms. *Phys. Rev. Lett.*, 105:123003.

[27] Chernobrod, B. M. and Berman, G. P. (2005). Spin microscope based on optically detected magnetic resonance. *Journal of applied physics*, 97(1):014903.

[28] Childress, L. and Hanson, R. (2013). Diamond nv centers for quantum computing and quantum networks. *MRS bulletin*, 38(2):134–138.

[29] Cleland, A. N. and Geller, M. R. (2004). Superconducting qubit storage and entanglement with nanomechanical resonators. *Physical review letters*, 93(7):070501.

[30] Davies, G. and Hamer, M. (1976). Optical studies of the 1.945 ev vibronic band in diamond. In *Proc. R. Soc. Lond. A*, volume 348, pages 285–298. The Royal Society.

[31] De Lange, G., Ristè, D., Dobrovitski, V., and Hanson, R. (2011). Single-spin magnetometry with multipulse sensing sequences. *Physical Review Letters*, 106(8):080802.

[32] De Lange, G., Wang, Z., Riste, D., Dobrovitski, V., and Hanson, R. (2010). Universal dynamical decoupling of a single solid-state spin from a spin bath. *Science*, 330(6000):60–63.

[33] Demirplak, M. and Rice, S. A. (2003). Adiabatic population transfer with control fields. *The Journal of Physical Chemistry A*, 107(46):9937–9945.

[34] Dobrovitski, V., Fuchs, G., Falk, A., Santori, C., and Awschalom, D. (2013). Quantum control over single spins in diamond. *Annu. Rev. Condens. Matter Phys.*, 4(1):23–50.

[35] Doherty, M., Dolde, F., Fedder, H., Jelezko, F., Wrachtrup, J., Manson, N., and Hollenberg, L. (2012). Theory of the ground-state spin of the nv- center in diamond. *Physical Review B*, 85(20):205203.

[36] Doherty, M. W., Manson, N. B., Delaney, P., and Hollenberg, L. C. (2011). The negatively charged nitrogen-vacancy centre in diamond: the electronic solution. *New Journal of Physics*, 13(2):025019.

[37] Doherty, M. W., Manson, N. B., Delaney, P., Jelezko, F., Wrachtrup, J., and Hollenberg, L. C. (2013). The nitrogen-vacancy colour centre in diamond. *Physics Reports*, 528(1):1–45.

[38] Dolde, F., Doherty, M. W., Michl, J., Jakobi, I., Naydenov, B., Pezzagna, S., Meijer, J., Neumann, P., Jelezko, F., Manson, N. B., et al. (2014). Nanoscale detection of a single fundamental charge in ambient conditions using the nv-center in diamond. *Physical review letters*, 112(9):097603.

[39] Dolde, F., Fedder, H., Doherty, M. W., Nöbauer, T., Rempp, F., Balasubramanian, G., Wolf, T., Reinhard, F., Hollenberg, L. C., Jelezko, F., et al. (2011). Electric-field sensing using single diamond spins. *Nature Physics*, 7(6):459.

[40] Du, J., Rong, X., Zhao, N., Wang, Y., Yang, J., and Liu, R. (2009). Preserving electron spin coherence in solids by optimal dynamical decoupling. *Nature*, 461(7268):1265.

[41] Dutt, M. G., Childress, L., Jiang, L., Togan, E., Maze, J., Jelezko, F., Zibrov, A., Hemmer, P., and Lukin, M. (2007). Quantum register based on individual electronic and nuclear spin qubits in diamond. *Science*, 316(5829):1312–1316.

[42] Fuchs, G., Burkard, G., Klimov, P., and Awschalom, D. (2011). A quantum memory intrinsic to single nitrogen-vacancy centres in diamond. *Nature Physics*, 7(10):789–793.

[43] Fuchs, G. D., Dobrovitski, V. V., Hanson, R., Batra, A., Weis, C. D., Schenkel, T., and Awschalom, D. D. (2008). Excited-state spectroscopy using single spin manipulation in diamond. *Phys. Rev. Lett.*, 101:117601.

[44] Gaebel, T., Domhan, M., Popa, I., Wittmann, C., Neumann, P., Jelezko, F., Rabeau, J. R., Stavrias, N., Greentree, A. D., Prawer, S., et al. (2006a). Room-temperature coherent coupling of single spins in diamond. *Nature Physics*, 2(6):408.

[45] Gaebel, T., Domhan, M., Wittmann, C., Popa, I., Jelezko, F., Rabeau, J., Greentree, A., Prawer, S., Trajkov, E., Hemmer, P. R., et al. (2006b). Photochromism in single nitrogen-vacancy defect in diamond. *Applied Physics B*, 82(2):243–246.

[46] Gaubatz, U., Rudecki, P., Becker, M., Schiemann, S., Külz, M., and Bergmann, K. (1988). Population switching between vibrational levels in molecular beams. *Chemical physics letters*, 149(5-6):463–468.

[47] Gaubatz, U., Rudecki, P., Schiemann, S., and Bergmann, K. (1990). Population transfer between molecular vibrational levels by stimulated raman scattering with partially overlapping laser fields. a new concept and experimental results. *The Journal of Chemical Physics*, 92(9):5363–5376.

[48] Gisin, N., Ribordy, G., Tittel, W., and Zbinden, H. (2002). Quantum cryptography. *Reviews of modern physics*, 74(1):145.

[49] Golter, D. A., Baldwin, T. K., and Wang, H. (2014). Protecting a solid-state spin from decoherence using dressed spin states. *Phys. Rev. Lett.*, 113:237601.

[50] Golter, D. A., Oo, T., Amezcua, M., Lekavicius, I., Stewart, K. A., and Wang, H. (2016a). Coupling a surface acoustic wave to an electron spin in diamond via a dark state. *Phys. Rev. X*, 6:041060.

[51] Golter, D. A., Oo, T., Amezcua, M., Stewart, K. A., and Wang, H. (2016b). Optomechanical quantum control of a nitrogen-vacancy center in diamond. *Phys. Rev. Lett.*, 116:143602.

[52] Golter, D. A. and Wang, H. (2014). Optically driven rabi oscillations and adiabatic passage of single electron spins in diamond. *Phys. Rev. Lett.*, 112:116403.

[53] Gordon Davies, I. (1994). Properties and growth of diamond. *INSPEC publication, Institution of Electrical Engineers*.

[54] Gruber, A., Dräbenstedt, A., Tietz, C., Fleury, L., Wrachtrup, J., and Von Borczyskowski, C. (1997). Scanning confocal optical microscopy and magnetic resonance on single defect centers. *Science*, 276(5321):2012–2014.

[55] Gustafsson, M. V., Aref, T., Kockum, A. F., Ekström, M. K., Johansson, G., and Delsing, P. (2014). Propagating phonons coupled to an artificial atom. *Science*, 346(6206):207–211.

[56] Häffner, H., Roos, C. F., and Blatt, R. (2008). Quantum computing with trapped ions. *Physics reports*, 469(4):155–203.

[57] Hahn, E. L. (1950). Spin echoes. *Phys. Rev.*, 80:580–594.

[58] Hall, L. T., Cole, J. H., Hill, C. D., and Hollenberg, L. C. (2009). Sensing of fluctuating nanoscale magnetic fields using nitrogen-vacancy centers in diamond. *Physical review letters*, 103(22):220802.

[59] Iakoubovskii, K., Adriaenssens, G., and Nesladek, M. (2000). Photochromism of vacancy-related centres in diamond. *Journal of Physics: Condensed Matter*, 12(2):189.

[60] Imamog, A., Awschalom, D. D., Burkard, G., DiVincenzo, D. P., Loss, D., Sherwin, M., Small, A., et al. (1999). Quantum information processing using quantum dot spins and cavity qed. *Physical review letters*, 83(20):4204.

[61] Ivanov, P., Vitanov, N., and Bergmann, K. (2004). Effect of dephasing on stimulated raman adiabatic passage. *Physical Review A*, 70(6):063409.

[62] Iwasaki, T., Ishibashi, F., Miyamoto, Y., Doi, Y., Kobayashi, S., Miyazaki, T., Tahara, K., Jahnke, K. D., Rogers, L. J., Naydenov, B., et al. (2015). Germanium-vacancy single color centers in diamond. *Scientific reports*, 5:12882.

[63] Jelezko, F., Gaebel, T., Popa, I., Domhan, M., Gruber, A., and Wrachtrup, J. (2004a). Observation of coherent oscillation of a single nuclear spin and realization of a two-qubit conditional quantum gate. *Phys. Rev. Lett.*, 93:130501.

[64] Jelezko, F., Gaebel, T., Popa, I., Gruber, A., and Wrachtrup, J. (2004b). Observation of coherent oscillations in a single electron spin. *Physical review letters*, 92(7):076401.

[65] Jelezko, F., Popa, I., Gruber, A., Tietz, C., Wrachtrup, J., Nizovtsev, A., and Kilin, S. (2002). Single spin states in a defect center resolved by optical spectroscopy. *Applied physics letters*, 81(12):2160–2162.

[66] Jelezko, F. and Wrachtrup, J. (2006). Single defect centres in diamond: A review. *physica status solidi (a)*, 203(13):3207–3225.

[67] Kane, B. E. (1998). A silicon-based nuclear spin quantum computer. *nature*, 393(6681):133.

[68] Kennedy, T., Colton, J., Butler, J., Linares, R., and Doering, P. (2003). Long coherence times at 300 k for nitrogen-vacancy center spins in diamond grown by chemical vapor deposition. *Applied Physics Letters*, 83(20):4190–4192.

[69] Kepesidis, K., Bennett, S., Portolan, S., Lukin, M. D., and Rabl, P. (2013). Phonon cooling and lasing with nitrogen-vacancy centers in diamond. *Physical Review B*, 88(6):064105.

[70] Kielpinski, D., Monroe, C., and Wineland, D. J. (2002). Architecture for a large-scale ion-trap quantum computer. *Nature*, 417(6890):709.

[71] Knill, E., Laflamme, R., and Milburn, G. J. (2001). A scheme for efficient quantum computation with linear optics. *nature*, 409(6816):46.

[72] Koehl, W. F., Buckley, B. B., Heremans, F. J., Calusine, G., and Awschalom, D. D. (2011). Room temperature coherent control of defect spin qubits in silicon carbide. *Nature*, 479(7371):84.

[73] Kolkowitz, S., Bleszynski Jayich, A. C., Unterreithmeier, Q. P., Bennett, S. D., Rabl, P., Harris, J. G. E., and Lukin, M. D. (2012a). Coherent sensing of a mechanical resonator with a single-spin qubit. *Science*, 335(6076):1603–1606.

[74] Kolkowitz, S., Jayich, A. C. B., Unterreithmeier, Q. P., Bennett, S. D., Rabl, P., Harris, J., and Lukin, M. D. (2012b). Coherent sensing of a mechanical resonator with a single-spin qubit. *Science*, 335(6076):1603–1606.

[75] Koppens, F., Buizert, C., Tielrooij, K.-J., Vink, I., Nowack, K., Meunier, T., Kouwenhoven, L., and Vandersypen, L. (2006). Driven coherent oscillations of a single electron spin in a quantum dot. *Nature*, 442(7104):766.

[76] Kubo, Y., Grezes, C., Dewes, A., Umeda, T., Isoya, J., Sumiya, H., Morishita, N., Abe, H., Onoda, S., Ohshima, T., et al. (2011). Hybrid quantum circuit with a superconducting qubit coupled to a spin ensemble. *Physical review letters*, 107(22):220501.

[77] Kucsko, G., Maurer, P., Yao, N. Y., Kubo, M., Noh, H., Lo, P., Park, H., and Lukin, M. D. (2013). Nanometre-scale thermometry in a living cell. *Nature*, 500(7460):54.

[78] Kurizki, G., Bertet, P., Kubo, Y., Mølmer, K., Petrosyan, D., Rabl, P., and Schmiedmayer, J. (2015). Quantum technologies with hybrid systems. *Proceedings of the National Academy of Sciences*, 112(13):3866–3873.

[79] Laucht, A., Kalra, R., Simmons, S., Dehollain, J. P., Muhonen, J. T., Mohiyaddin, F. A., Freer, S., Hudson, F. E., Itoh, K. M., Jamieson, D. N., McCallum, J. C., Dzurak, A. S., and Morello, A. (2017). A dressed spin qubit in silicon. *Nature nanotechnology*, 12(1):61.

[80] Le Sage, D., Arai, K., Glenn, D., DeVience, S., Pham, L., Rahn-Lee, L., Lukin, M., Yacoby, A., Komeili, A., and Walsworth, R. (2013). Optical magnetic imaging of living cells. *Nature*, 496(7446):486.

[81] Lecocq, F., Clark, J. B., Simmonds, R. W., Aumentado, J., and Teufel, J. D. (2015). Quantum nondemolition measurement of a nonclassical state of a massive object. *Phys. Rev. X*, 5:041037.

[82] Lee, D., Lee, K. W., Cady, J. V., Ovartchaiyapong, P., and Jayich, A. C. B. (2017). Topical review: Spins and mechanics in diamond. *Journal of Optics*, 19(3):033001.

[83] Leibfried, D., Blatt, R., Monroe, C., and Wineland, D. (2003a). Quantum dynamics of single trapped ions. *Reviews of Modern Physics*, 75(1):281.

[84] Leibfried, D., Blatt, R., Monroe, C., and Wineland, D. (2003b). Quantum dynamics of single trapped ions. *Rev. Mod. Phys.*, 75:281–324.

[85] Lenef, A. and Rand, S. (1996). Electronic structure of the n-v center in diamond: Theory. *Physical Review B*, 53(20):13441.

[86] Lesik, M., Spinicelli, P., Pezzagna, S., Happel, P., Jacques, V., Salord, O., Rasser, B., Delobbe, A., Sudraud, P., Tallaire, A., et al. (2013). Maskless and targeted creation of arrays of colour centres in diamond using focused ion beam technology. *physica status solidi (a)*, 210(10):2055–2059.

[87] Linke, N. M., Maslov, D., Roetteler, M., Debnath, S., Figgatt, C., Landsman, K. A., Wright, K., and Monroe, C. (2017). Experimental comparison of two quantum computing architectures. *Proceedings of the National Academy of Sciences*, page 201618020.

[88] London, P., Scheuer, J., Cai, J.-M., Schwarz, I., Retzker, A., Plenio, M. B., Katagiri, M., Teraji, T., Koizumi, S., Isoya, J., Fischer, R., McGuinness, L. P., Naydenov, B., and Jelezko, F. (2013). Detecting and polarizing nuclear spins with double resonance on a single electron spin. *Phys. Rev. Lett.*, 111:067601.

[89] Loss, D. and DiVincenzo, D. P. (1998). Quantum computation with quantum dots. *Phys. Rev. A*, 57:120–126.

[90] MacQuarrie, E., Gosavi, T., Moehle, A., Jungwirth, N., Bhave, S., and Fuchs, G. (2015a). Coherent control of a nitrogen-vacancy center spin ensemble with a diamond mechanical resonator. *Optica*, 2(3):233–238.

[91] MacQuarrie, E. R., Gosavi, T. A., Bhave, S. A., and Fuchs, G. D. (2015b). Continuous dynamical decoupling of a single diamond nitrogen-vacancy center spin with a mechanical resonator. *Phys. Rev. B*, 92:224419.

[92] MacQuarrie, E. R., Gosavi, T. A., Jungwirth, N. R., Bhave, S. A., and Fuchs, G. D. (2013). Mechanical spin control of nitrogen-vacancy centers in diamond. *Phys. Rev. Lett.*, 111:227602.

[93] Majer, J., Chow, J., Gambetta, J., Koch, J., Johnson, B., Schreier, J., Frunzio, L., Schuster, D., Houck, A., Wallraff, A., et al. (2007). Coupling superconducting qubits via a cavity bus. *Nature*, 449(7161):443.

[94] Manson, N. and Harrison, J. (2005). Photo-ionization of the nitrogen-vacancy center in diamond. *Diamond and related materials*, 14(10):1705–1710.

[95] Manson, N. B., Harrison, J. P., and Sellars, M. J. (2006). Nitrogen-vacancy center in diamond: Model of the electronic structure and associated dynamics. *Phys. Rev. B*, 74:104303.

[96] Maurer, P. C., Kucsko, G., Latta, C., Jiang, L., Yao, N. Y., Bennett, S. D., Pastawski, F., Hunger, D., Chisholm, N., Markham, M., et al. (2012). Room-temperature quantum bit memory exceeding one second. *Science*, 336(6086):1283–1286.

[97] Maze, J., Gali, A., Togan, E., Chu, Y., Trifonov, A., Kaxiras, E., and Lukin, M. (2011). Properties of nitrogen-vacancy centers in diamond: the group theoretic approach. *New Journal of Physics*, 13(2):025025.

[98] Meesala, S., Sohn, Y.-I., Atikian, H. A., Kim, S., Burek, M. J., Choy, J. T., and Lončar, M. (2016). Enhanced strain coupling of nitrogen-vacancy spins to nanoscale diamond cantilevers. *Physical Review Applied*, 5(3):034010.

[99] Meiboom, S. (1958). S. meiboom and d. gill, rev. sci. instrum. 29, 688 (1958). *Rev. Sci. Instrum.*, 29:688.

[100] Meijer, J., Burchard, B., Domhan, M., Wittmann, C., Gaebel, T., Popa, I., Jelezko, F., and Wrachtrup, J. (2005). Generation of single color centers by focused nitrogen implantation. *Applied Physics Letters*, 87(26):261909.

[101] Metcalfe, M. (2014). Applications of cavity optomechanics. *Applied Physics Reviews*, 1(3):031105.

[102] Mollow, B. (1969). Power spectrum of light scattered by two-level systems. *Physical Review*, 188(5).

[103] Monroe, C. and Kim, J. (2013). Scaling the ion trap quantum processor. *Science*, 339(6124):1164–1169.

[104] Morgan, D. (1973). Surface acoustic wave devices and applications: 1. introductory review. *Ultrasonics*, 11(3):121–131.

[105] Naydenov, B., Dolde, F., Hall, L. T., Shin, C., Fedder, H., Hollenberg, L. C., Jelezko, F., and Wrachtrup, J. (2011). Dynamical decoupling of a single-electron spin at room temperature. *Physical Review B*, 83(8):081201.

[106] Neumann, P., Jakobi, I., Dolde, F., Burk, C., Reuter, R., Waldherr, G., Honert, J., Wolf, T., Brunner, A., Shim, J. H., et al. (2013). High-precision nanoscale temperature sensing using single defects in diamond. *Nano letters*, 13(6):2738–2742.

[107] Neumann, P., Mizuochi, N., Rempp, F., Hemmer, P., Watanabe, H., Yamasaki, S., Jacques, V., Gaebel, T., Jelezko, F., and Wrachtrup, J. (2008). Multipartite entanglement among single spins in diamond. *science*, 320(5881):1326–1329.

[108] O'brien, J. L. (2007). Optical quantum computing. *Science*, 318(5856):1567–1570.

[109] O'Connell, A. D., Hofheinz, M., Ansmann, M., Bialczak, R. C., Lenander, M., Lucero, E., Neeley, M., Sank, D., Wang, H., Weides, M., et al. (2010). Quantum ground state and single-phonon control of a mechanical resonator. *Nature*, 464(7289):697.

[110] Ohno, K., Joseph Heremans, F., de las Casas, C. F., Myers, B. A., Alemán, B. J., Bleszynski Jayich, A. C., and Awschalom, D. D. (2014). Three-dimensional localization of spins in diamond using 12c implantation. *Applied Physics Letters*, 105(5):052406.

[111] Oo, T. H. (2017). *Coupling Nitrogen Vacancy Centers in Diamond to A Nanomechanical Oscillator*. PhD thesis, University of Oregon.

[112] Ovartchaiyapong, P., Lee, K. W., Myers, B. A., and Jayich, A. C. B. (2014). Dynamic strain-mediated coupling of a single diamond spin to a mechanical resonator. *Nature communications*, 5:4429.

[113] Peterson, R. W., Purdy, T. P., Kampel, N. S., Andrews, R. W., Yu, P.-L., Lehnert, K. W., and Regal, C. A. (2016). Laser cooling of a micromechanical membrane to the quantum backaction limit. *Phys. Rev. Lett.*, 116:063601.

[114] Petersson, K. D., McFaul, L. W., Schroer, M. D., Jung, M., Taylor, J. M., Houck, A. A., and Petta, J. R. (2012). Circuit quantum electrodynamics with a spin qubit. *Nature*, 490(7420):380.

[115] Pezzagna, S., Naydenov, B., Jelezko, F., Wrachtrup, J., and Meijer, J. (2010). Creation efficiency of nitrogen-vacancy centres in diamond. *New Journal of Physics*, 12(6):065017.

[116] Pham, L. M., Bar-Gill, N., Belthangady, C., Le Sage, D., Cappellaro, P., Lukin, M. D., Yacoby, A., and Walsworth, R. L. (2012). Enhanced solid-state multispin metrology using dynamical decoupling. *Physical Review B*, 86(4):045214.

[117] Pla, J. J., Tan, K. Y., Dehollain, J. P., Lim, W. H., Morton, J. J., Jamieson, D. N., Dzurak, A. S., and Morello, A. (2012). A single-atom electron spin qubit in silicon. *Nature*, 489(7417):541.

[118] Press, D., Ladd, T. D., Zhang, B., and Yamamoto, Y. (2008). Complete quantum control of a single quantum dot spin using ultrafast optical pulses. *Nature*, 456(7219):218.

[119] Rabeau, J., Huntington, S., Greentree, A., and Prawer, S. (2005). Diamond chemical-vapor deposition on optical fibers for fluorescence waveguiding. *Applied Physics Letters*, 86(13):134104.

[120] Rabeau, J., Reichart, P., Tamanyan, G., Jamieson, D., Prawer, S., Jelezko, F., Gaebel, T., Popa, I., Domhan, M., and Wrachtrup, J. (2006). Implantation of labelled single nitrogen vacancy centers in diamond using n 15. *Applied Physics Letters*, 88(2):023113.

[121] Rabl, P., Cappellaro, P., Dutt, M. V. G., Jiang, L., Maze, J. R., and Lukin, M. D. (2009). Strong magnetic coupling between an electronic spin qubit and a mechanical resonator. *Phys. Rev. B*, 79:041302.

[122] Rabl, P., Kolkowitz, S. J., Koppens, F., Harris, J., Zoller, P., and Lukin, M. D. (2010). A quantum spin transducer based on nanoelectromechanical resonator arrays. *Nature Physics*, 6(8):602.

[123] Robledo, L., Bernien, H., van Weperen, I., and Hanson, R. (2010). Control and coherence of the optical transition of single nitrogen vacancy centers in diamond. *Physical review letters*, 105(17):177403.

[124] Rogers, L., McMurtrie, R., Sellars, M., and Manson, N. (2009). Time-averaging within the excited state of the nitrogen-vacancy centre in diamond. *New Journal of Physics*, 11(6):063007.

[125] Rogers, L. J., Doherty, M. W., Barson, M. S., Onoda, S., Ohshima, T., and Manson, N. B. (2015). Singlet levels of the nv- centre in diamond. *New Journal of Physics*, 17(1):013048.

[126] Rogers, L. J., Jahnke, K. D., Metsch, M. H., Sipahigil, A., Binder, J. M., Teraji, T., Sumiya, H., Isoya, J., Lukin, M. D., Hemmer, P., and Jelezko, F. (2014). All-optical initialization, readout, and coherent preparation of single silicon-vacancy spins in diamond. *Phys. Rev. Lett.*, 113:263602.

[127] Ryan, C., Hodges, J., and Cory, D. (2010). Robust decoupling techniques to extend quantum coherence in diamond. *Physical Review Letters*, 105(20):200402.

[128] Santori, C., Fattal, D., Spillane, S. M., Fiorentino, M., Beausoleil, R. G., Greentree, A. D., Olivero, P., Draganski, M., Rabeau, J. R., Reichart, P., Gibson, B. C., Rubanov, S., Jamieson, D. N., and Prawer, S. (2006a). Coherent population trapping in diamond n-v centers at zero magnetic field. *Opt. Express*, 14(17):7986–7994.

[129] Santori, C., Tamarat, P., Neumann, P., Wrachtrup, J., Fattal, D., Beausoleil, R. G., Rabeau, J., Olivero, P., Greentree, A. D., Prawer, S., Jelezko, F., and Hemmer, P. (2006b). Coherent population trapping of single spins in diamond under optical excitation. *Phys. Rev. Lett.*, 97:247401.

[130] Schoelkopf, R. and Girvin, S. (2008). Wiring up quantum systems. *Nature*, 451(7179):664.

[131] Schuetz, M. J. A., Kessler, E. M., Giedke, G., Vandersypen, L. M. K., Lukin, M. D., and Cirac, J. I. (2015). Universal quantum transducers based on surface acoustic waves. *Phys. Rev. X*, 5:031031.

[132] Shiokawa, S. and Kondoh, J. (2004). Surface acoustic wave sensors. *Japanese journal of applied physics*, 43(5S):2799.

[133] Sipahigil, A., Goldman, M. L., Togan, E., Chu, Y., Markham, M., Twitchen, D. J., Zibrov, A. S., Kubanek, A., and Lukin, M. D. (2012). Quantum interference of single photons from remote nitrogen-vacancy centers in diamond. *Physical review letters*, 108(14):143601.

[134] Sipahigil, A., Jahnke, K. D., Rogers, L. J., Teraji, T., Isoya, J., Zibrov, A. S., Jelezko, F., and Lukin, M. D. (2014). Indistinguishable photons from separated silicon-vacancy centers in diamond. *Physical review letters*, 113(11):113602.

[135] Siyushev, P., Metsch, M. H., Ijaz, A., Binder, J. M., Bhaskar, M. K., Sukachev, D. D., Sipahigil, A., Evans, R. E., Nguyen, C. T., Lukin, M. D., Hemmer, P. R., Palyanov, Y. N., Kupriyanov, I. N., Borzdov, Y. M., Rogers, L. J., and Jelezko, F. (2017). Optical and microwave control of germanium-vacancy center spins in diamond. *Phys. Rev. B*, 96:081201.

[136] Stark, A., Aharon, N., Unden, T., Louzon, D., Huck, A., Retzker, A., Andersen, U. L., and Jelezko, F. (2017). Narrow-bandwidth sensing of high-frequency fields with continuous dynamical decoupling. *Nature communications*, 8(1):1105.

[137] Steinert, S., Dolde, F., Neumann, P., Aird, A., Naydenov, B., Balasubramanian, G., Jelezko, F., and Wrachtrup, J. (2010). High sensitivity magnetic imaging using an array of spins in diamond. *Review of scientific instruments*, 81(4):043705.

[138] Tamarat, P., Manson, N., Harrison, J., McMurtrie, R., Nizovtsev, A., Santori, C., Beausoleil, R., Neumann, P., Gaebel, T., Jelezko, F., et al. (2008). Spin-flip and spin-conserving optical transitions of the nitrogen-vacancy centre in diamond. *New Journal of Physics*, 10(4):045004.

[139] Taylor, J., Cappellaro, P., Childress, L., Jiang, L., Budker, D., Hemmer, P., Yacoby, A., Walsworth, R., and Lukin, M. (2008). High-sensitivity diamond magnetometer with nanoscale resolution. *Nature Physics*, 4(10):810.

[140] Teissier, J., Barfuss, A., Appel, P., Neu, E., and Maletinsky, P. (2014). Strain coupling of a nitrogen-vacancy center spin to a diamond mechanical oscillator. *Phys. Rev. Lett.*, 113:020503.

[141] Teissier, J., Barfuss, A., and Maletinsky, P. (2017). Hybrid continuous dynamical decoupling: a photon-phonon doubly dressed spin. *Journal of Optics*, 19(4):044003.

[142] Tian, L., Rabl, P., Blatt, R., and Zoller, P. (2004). Interfacing quantum-optical and solid-state qubits. *Physical review letters*, 92(24):247902.

[143] Timoney, N., Baumgart, I., Johanning, M., Varón, A., Plenio, M., Retzker, A., and Wunderlich, C. (2011). Quantum gates and memory using microwave-dressed states. *Nature*, 476(7359):185.

[144] Toyli, D. M., Charles, F., Christle, D. J., Dobrovitski, V. V., and Awschalom, D. D. (2013). Fluorescence thermometry enhanced by the quantum coherence of single spins in diamond. *Proceedings of the National Academy of Sciences*, 110(21):8417–8421.

[145] Uhrig, G. S. (2007). Gs uhrig, phys. rev. lett. 98, 100504 (2007). *Phys. Rev. Lett.*, 98:100504.

[146] Unanyan, R., Yatsenko, L., Bergmann, K., and Shore, B. (1997). Laser-induced adiabatic atomic reorientation with control of diabatic losses. *Optics communications*, 139(1-3):48–54.

[147] Underwood, M., Mason, D., Lee, D., Xu, H., Jiang, L., Shkarin, A. B., Børkje, K., Girvin, S. M., and Harris, J. G. E. (2015). Measurement of the motional sidebands of a nanogram-scale oscillator in the quantum regime. *Phys. Rev. A*, 92:061801.

[148] Vallone, G., Pomarico, E., Mataloni, P., De Martini, F., and Berardi, V. (2007). Realization and characterization of a two-photon four-qubit linear cluster state. *Physical review letters*, 98(18):180502.

[149] Van der Sar, T., Wang, Z., Blok, M., Bernien, H., Taminiau, T., Toyli, D., Lidar, D., Awschalom, D., Hanson, R., and Dobrovitski, V. (2012). Decoherence-protected quantum gates for a hybrid solid-state spin register. *Nature*, 484(7392):82.

[150] Van Oort, E., Manson, N., and Glasbeek, M. (1988). Optically detected spin coherence of the diamond nv centre in its triplet ground state. *Journal of Physics C: Solid State Physics*, 21(23):4385.

[151] Vasilev, G., Kuhn, A., and Vitanov, N. (2009). Optimum pulse shapes for stimulated raman adiabatic passage. *Physical Review A*, 80(1):013417.

[152] Vitanov, N. V., Rangelov, A. A., Shore, B. W., and Bergmann, K. (2017). Stimulated raman adiabatic passage in physics, chemistry, and beyond. *Rev. Mod. Phys.*, 89:015006.

[153] Wallraff, A., Schuster, D. I., Blais, A., Frunzio, L., Huang, R.-S., Majer, J., Kumar, S., Girvin, S. M., and Schoelkopf, R. J. (2004). Strong coupling of a single photon to a superconducting qubit using circuit quantum electrodynamics. *Nature*, 431(7005):162.

[154] Wang, C.-F., Hanson, R., Awschalom, D., Hu, E., Feygelson, T., Yang, J., and Butler, J. (2007). Fabrication and characterization of two-dimensional photonic crystal microcavities in nanocrystalline diamond. *Applied Physics Letters*, 91(20):201112.

[155] Wang, Z.-H., De Lange, G., Ristè, D., Hanson, R., and Dobrovitski, V. (2012). Comparison of dynamical decoupling protocols for a nitrogen-vacancy center in diamond. *Physical Review B*, 85(15):155204.

[156] Wang, Z.-Y., Cai, J.-M., Retzker, A., and Plenio, M. B. (2014). All-optical magnetic resonance of high spectral resolution using a nitrogen-vacancy spin in diamond. *New Journal of Physics*, 16(8):083033.

[157] Weiß, M., Kapfinger, S., Reichert, T., Finley, J. J., Wixforth, A., Kaniber, M., and Krenner, H. J. (2016). Surface acoustic wave regulated single photon emission from a coupled quantum dot–nanocavity system. *Applied Physics Letters*, 109(3):033105.

[158] Wineland, D. J. (2013). Nobel lecture: Superposition, entanglement, and raising schrödinger's cat. *Rev. Mod. Phys.*, 85:1103–1114.

[159] Wrachtrup, J. and Jelezko, F. (2006). Processing quantum information in diamond. *Journal of Physics: Condensed Matter*, 18(21):S807.

[160] Wu, F., Grove, R., and Ezekiel, S. (1975). Investigation of the spectrum of resonance fluorescence induced by a monochromatic field. *Physical Review Letters*, 35(21):1426.

[161] Xu, X., Wang, Z., Duan, C., Huang, P., Wang, P., Wang, Y., Xu, N., Kong, X., Shi, F., Rong, X., and Du, J. (2012). Coherence-protected quantum gate by continuous dynamical decoupling in diamond. *Phys. Rev. Lett.*, 109:070502.

[162] Zhou, B. B., Baksic, A., Ribeiro, H., Yale, C. G., Heremans, F. J., Jerger, P. C., Auer, A., Burkard, G., Clerk, A. A., and Awschalom, D. D. (2017). Accelerated quantum control using superadiabatic dynamics in a solid-state lambda system. *Nature Physics*, 13(4):330.